POLITECNICO DI TORINO
Repository ISTITUZIONALE

Tailoring sub-5 nm Fe-doped CeO2 nanocrystals within confined spaces to boost photocatalytic hydrogen evolution under visible light

Original
Tailoring sub-5 nm Fe-doped CeO2 nanocrystals within confined spaces to boost photocatalytic hydrogen evolution under visible light / Iervolino, G., Tammaro, O., Fontana, M., Masenelli, B., Lamirand, A.D., Vaiano, V., Esposito, S.. - In: JOURNAL OF ENERGY CHEMISTRY. - ISSN 2095-4956. - 101:(2025), pp. 263-277. [10.1016/j.jechem.2024.09.041]

Availability:
This version is available at: 11583/2993328 since: 2024-11-08T13:08:55Z

Publisher:
Elsevier

Published
DOI:10.1016/j.jechem.2024.09.041

Terms of use:

This article is made available under terms and conditions as specified in the corresponding bibliographic description in the repository

Publisher copyright
Elsevier postprint/Author's Accepted Manuscript

© 2025. This manuscript version is made available under the CC-BY-NC-ND 4.0 license
http://creativecommons.org/licenses/by-nc-nd/4.0/.The final authenticated version is available online at:
http://dx.doi.org/10.1016/j.jechem.2024.09.041

(Article begins on next page)

10 November 2026

Tailoring sub-5 nm Fe-doped CeO_2 nanocrystals within confined spaces to boost photocatalytic hydrogen evolution under visible light

Giuseppina Iervolino[a], Olimpia Tammaro[b], Marco Fontana[b,c], Bruno Masenelli[d], Anne D. Lamirand[d], Vincenzo Vaiano[a]*, Serena Esposito[b]*

[a] Department of Industrial Engineering, University of Salerno, Via Giovanni Paolo II 132, 84084 Fisciano (SA), Italy

[b] Department of Applied Science and Technology and INSTM Unit of Torino – Politecnico, Politecnico di Torino, Corso Duca degli Abruzzi 24, 10129 Torino, Italy.

[c] Center for Sustainable Future Technologies @POLITO, Istituto Italiano di Tecnologia, Via Livorno 60, Turin 10144, Italy

[d] INSA Lyon, Ecole Centrale de Lyon, CNRS, Universite Claude Bernard Lyon 1, CPE Lyon, INL, UMR5270, 69621 Villeurbanne, France

Corresponding authors: vvaiano@unisa.it (V. Vaiano), serena_esposito@polito.it (S. Esposito).

Abstract

This work aimed to study the efficiency of the reverse micelle (RM) preparation route in the syntheses of sub-5 nm Fe-doped CeO_2 nanocrystals for boosting the visible-light-driven photocatalytic hydrogen production from methanol aqueous solutions. The effectiveness of confining precipitation reactions within micellar cages was evaluated through extensive physicochemical characterization. In particular, the nominal composition (0-5 mol % Fe) was preserved as ascertained by ICP-MS analysis, and the absence of separate iron-containing crystalline phases was supported by X-ray diffraction. The effective aliovalent doping and modulation of the optical properties were investigated using UV-Vis, Raman and photoluminescence spectroscopies. 2.5 mol % iron was found to be an optimal content to achieve a significant decrease in the band gap, enhance the concentration of oxygen vacancy defects, and increase the charge carrier lifetime. The photocatalytic activity of Fe-doped CeO_2 prepared at different Fe contents with RM preparation was studied and compared with undoped CeO_2. The optimal iron load was identified to be 2.5 mol%, achieving the highest hydrogen production (7566 μmol L^{-1} after 240 min under visible light). Moreover, for comparison, the conventional precipitation (P) method was adopted to prepare iron containing CeO_2 at the optimal content (2.5 mol% Fe). The Fe-doped CeO_2 catalyst prepared by RM showed a significantly higher hydrogen production than that obtained with the sample prepared by the P method. The optimal Fe-doped CeO_2, prepared by the RM method, was stable for six reuse cycles. Moreover, the role of water in the mechanism of photocatalytic hydrogen evolution under visible light was studied through the test in the presence of D_2O. The obtained results evidenced that hydrogen was produced from the reduction of H^+ by the electrons promoted in the conduction band, while methanol was preferentially oxidized by the photogenerated positive holes.

Keywords: sub-5 nm Fe-doped CeO_2; hydrogen evolution; photocatalysis; visible light; reverse micelles; mesoporous CeO_2

1. Introduction

The global demand for sustainable and clean energy sources has led to considerable interest in hydrogen as a versatile and environmentally friendly fuel. Hydrogen, with its high energy content and absence of carbon emissions when used in fuel cells, stands out as a promising alternative to fossil fuels. Among various hydrogen production methods, photocatalytic water splitting has emerged as particularly attractive due to its potential to harness solar energy, one of the most abundant and renewable energy sources available [1, 2]. Photocatalytic water splitting involves the conversion of water into hydrogen and oxygen using light energy and a suitable semiconductor as a photocatalyst. The efficiency and feasibility of this reaction are highly dependent on the properties of the photocatalyst and on the use of sacrificial agents in the reaction medium able to be oxidized by the positive holes, so reducing the recombination phenomena of photoinduced charge carriers [3-5]. Compared to other sacrificial agents, methanol can effectively capture the positive holes in the semiconductor valence band, limiting the charge carriers recombination phenomena and, consequently, making the electrons promoted in the conduction band available to reduce H^+ to H_2 [6, 7]. Therefore, methanol is considered the model molecule for assessing the ability of photocatalysts in hydrogen photoproduction [8].

Semiconductors such as titanium dioxide (TiO_2), zinc oxide (ZnO), and more recently, materials like graphitic carbon nitride (g-C_3N_4) and perovskites, have been extensively studied and modified to improve their photocatalytic performance in the water splitting reaction [9-13]. Strategies such as doping with metal or non-metal ions, creation of heterojunctions, and co-catalyst integration resulted in increasing light absorption, improving charge-carrier separation, and reducing recombination rates thereof [14-19]. Furthermore, surface modifications and the development of new composite materials can be viable solutions to further optimize the photocatalytic process [20-22]**.**

In the last years, cerium oxide (CeO_2), a rare-earth metal oxide, has emerged as a promising photocatalyst due to its unique electronic structure, high oxygen storage capacity, and excellent stability [23]. The optical band gap of CeO_2 (~3.2 eV) can be modified through various approaches to improve its absorption of visible light and enhance the photoproduction of hydrogen from aqueous

solutions [24, 25]. Noticeably, doping with metal elements (such as rare earth and transition metal cations) appears the most promising for the formulation of visible light-active CeO_2-based photocatalysts [25-29].

Although doping of the crystalline structure of cerium oxide with metal cations has led to a significant improvement in the photocatalytic performance in the presence of visible light, it is not easy to propose and realize the large-scale production of these photocatalysts due to the scarcity and high cost of most of the doping metals proposed in the literature [30]. On the other hand, the iron element is significantly cheaper than rare earth and other transition metals [30]. Therefore, the formulation of Fe-doped CeO_2 photocatalysts currently seems to be a promising strategy to solve the problems that emerged in the research dedicated to the preparation of visible light-activated CeO_2 photocatalysts. Moreover, doping with iron can induce an enhanced synergistic effect between redox couple of the cerium (Ce^{4+}/Ce^{3+}) and iron cations (Fe^{3+}/Fe^{2+}) [31].

Concerning the photocatalytic hydrogen evolution under visible light, it is worthwhile to note that the number of literature papers dealing with the Fe-doped CeO_2 catalysts is still scarce. Recently, Mansingh et al. proposed a novel approach to prepare Fe-doped CeO_2 by co-precipitation method, showing that the doping with Fe reduced the band gap energy from 3.0 eV up to 1.85 eV and with a photocatalysts particle size higher than 7 nm [31]. Moreover, the results in terms of photocatalytic hydrogen production from methanol aqueous solutions evidenced that only 3 wt% Fe loading was enough to achieve the best H_2 production under visible light irradiation and better photostability [31]. Despite such promising advancements, several challenges remain in optimizing Fe-doped CeO_2 photocatalysts for efficient hydrogen production under visible light. Indeed, behind the beneficial effect of iron doping in ceria photocatalysts there is a complex interplay of several parameters, mostly arising from the amount of iron content related to its effective inclusion and distribution in the ceria lattice and the type of doping sites. The synthesis route has, indeed, a significant impact on the properties of nanocatalysts, opening a long debate on the effective enrichment of the ceria structure with iron heteroatoms, whether substitutional or interstitial and their actual contribution and role in

catalyst efficiency. The reported speculations are further complicated by the presence and density of defects. In this scenario, many of the challenges concerning optimal catalyst characteristics are not overcome by traditional preparation methods, which mainly suffer from poor control of synthesis parameters, low reproducibility, and harsh operating conditions [32, 33]. In this work, a versatile and reliable synthesis protocol was developed exploiting the benefits and recognized potential of the one-pot reverse micelles approach [34-36]. Using this approach, reactions that usually take place in aqueous media are channeled into the confined space of the reverse micelles core. The monodisperse, nanometre-sized water droplets contained in these micelles are ideal reactors for controlling the nucleation and growth of nanoparticles. The cage-like environment provided by the microemulsion with the simultaneous presence of cerium and dopant precursors will favor an excellent control of the final powder stoichiometry with the possibility of obtaining homogeneity and mixing at the atomic scale, ultimately favoring the effective inclusion of heteroatoms in large(r) amounts.

This method, therefore, retains the simplicity of the co-precipitation method but overcomes its limitation of poor control over nanoparticle formation.

Moreover, another key aspect to be considered is that the photocatalytic activity and stability are significantly improved if photocatalysts characterized by ultra-small nanocrystals (below 5 nm) are obtained in a manner that fruitful the quantum confinement effects [30, 37]. In this perspective, the modification of nanoparticle size can be achieved through the reverse micelle approach by varying the synthesis conditions, in particular the type and nature of the surfactant and the water/surfactant ratio [38]. Based on such observations, this paper aims to study the efficiency of the reverse micelle preparation route in the synthesis of Fe-doped CeO_2 at different iron content for the visible-light-driven hydrogen production from methanol aqueous solutions. If the purpose of doping is relatively straightforward, understanding the structure/composition-activity relationship of Fe-doped CeO_2 in the photocatalytic production of H_2 by water splitting still needs to be addressed. To meet this need, an in-depth characterization was conducted to identify the structural, textural and morphological properties, as well as the optical properties, of the prepared materials. The photocatalytic activity of

the Fe-doped CeO_2 prepared at different Fe content was assessed and compared with undoped CeO_2. Moreover, the photocatalytic results obtained with the doped photocatalysts prepared via the reverse micelle approach were compared with the Fe-doped CeO_2 prepared with the conventional precipitation method. Catalytic test results were critically discussed in correlation with chemical-physical properties and a possible reaction mechanism was proposed. Finally, the stability of the best photocatalyst was demonstrated through reusability tests. To our knowledge, there are no available literature papers dealing with boosting photocatalytic hydrogen evolution under visible light using Fe-doped CeO_2 prepared via the reverse micelle method.

2. Experimental

Cyclohexane (ACS reagent ≥ 99.5 %), cerium nitrate hexahydrate, iron chloride (reagent grade 97 %), ammonia (ACS reagent 28–30 %), 1-butanol (ACS reagent ≥ 99.4 %), polyoxyethylene (10) cetyl ether (BrijC10), ethanol (≥ 99.8 %) and methanol (≥ 99.9 %) were purchased by Sigma-Aldrich and used without further modification. Bi-distilled water has been used for the preparation of salt solution.

2.1 *Synthesis by reverse micelle method*

In a typical synthesis [24, 35], 8.2 g of surfactant (Brij C10) was dissolved in 100 mL of cyclohexane under stirring at room temperature. 0.5 M aqueous solution of cerium and iron salts is slowly added dropwise to the oil phase to obtain appropriate water-in-oil (w/o) micelles. The volume of the aqueous precursor solution was selected to obtain a w0 value of 25 (w0 is defined as the water-surfactant molar ratio). 4 mL of co-surfactant (1-butanol) was added to preserve the optical transparency of the emulsion, avoiding the formation of flocculates. Finally, 5.4 mL of ammonia solution (precipitating agent) is slowly dripped. The mixture is stirred for 1.5 h at room temperature. The solid phase is then collected by centrifugation, washed twice with ethanol, and dried under a hood for 2 days. The dried

powder was calcinated at 120 °C for 6 h. The samples are labeled as Fe(x%)-CeO_2 RM, where x represents the nominal molar percentage of iron and RM stands for reverse micelle. The amounts of iron were calculated to obtain nominal molar % of iron equal to 0 mol %, 1.0 mol %, 1.5 mol %, 2.5 mol %, and 5 mol%. Samples Fe(2.5%)-CeO_2 RM after six cycles of photocatalytic reaction were labeled as Fe(2.5%)-CeO_2 RM_spent.

2.2 *Synthesis by precipitation*

For comparison, a conventional precipitation was adopted to prepare the Fe-CeO_2 catalysts. Firstly, proper amounts of cerium and iron precursors were dissolved in deionized water, until a 0.5 M cations total concentration was reached. Then, a proper amount of ammonia solution (precipitating agent) was slowly added. The mixture was vigorously stirred for 15 min to ensure a complete co-precipitation. The solid phase is then collected by centrifugation, washed twice with ethanol, and dried under a hood for 2 days. The dried powder was calcinated at 120 °C for 6 h. The amounts of cerium and iron were calculated to obtain a nominal composition expressed as a molar % of iron equal to 0 mol % and 2.5 mol %. The samples are labeled as Fe(x%)-CeO_2 P where x represents the nominal molar percentage of iron and P stands for precipitation.

2.3. *Structural, morphological and surface characterization*

The effective compositions of the prepared catalysts, expressed as Fe/Ce molar ratio, were assessed by Inductively Coupled Plasma Mass Spectrometry (ICP-MS) analysis (ICAPQ Thermo Scientific). The adopted protocols for the ICP-MS measurement include before the analysis, an extraction process with a hot nitric acid solution to ensure complete dissolution of the interest elements.

The X-ray Diffraction (XRD) analysis of the powder samples was conducted using an X'Pert Philips diffractometer equipped with Cu Kα radiation, covering a 2θ range of 5 °– 90 ° at a step width of

0.026 ° and time per step of 200 s. The patterns obtained from this analysis were matched with entries from the PDF-2 Release 2002 database for identification. The lattice parameters of the fluorite phase present in the samples were determined through unit cell refinement using UnitCell software and the crystallite size was determined by applying the Scherrer formula.

The optical properties of the powder samples were evaluated by UV-Vis diffuse reflectance (DR) and Photo Luminescence (PL) spectroscopies. For the UV-Vis analysis the spectra were recorded on a UV − Vis Varian Cary 5000 spectrophotometer equipped with a DR integration sphere (200–600 nm range). The indirect band gap values of the samples were determined by fitting the UV-Vis data with the Tauc plot method referring to the formula $(F(R)h\nu)^{1/2} = f(h\nu)$.

The PL spectra were collected employing a Perkin Elmer Spectrofluorometer LS55. The spectra were recorded in the range of 350- 550 nm with an excitation wavelength λ_{ex} = 285 nm and slits 10 nm.

The prepared samples were characterized also in terms of textural properties through N_2 physisorption and desorption at -196 °C (ASAP 2020, Micrometrics Instruments.). Before the measurement, the sample was outgassed under a high vacuum at 150 °C for 3 h to remove pollutants previously adsorbed. Key textural features were extrapolated from isotherm data: the specific surface area (SSA) of the samples was calculated according to the BET (Brunauer–Emmet–Teller), total pore volume was determined from the amount of adsorbed N_2 in the p/p° range from 0.9 up to 0.98. The Barrett–Joyner–Halenda (BJH) approach was used to calculate the pore size distribution of the sample using the desorption data.

Raman spectroscopy was used to investigate the crystalline quality of the samples, namely the crystalline phase, and provide a semi-quantitative analysis of the oxygen vacancy content. The spectra were acquired at room temperature using a LabRAM HR spectrometer (Jobin Yvon-Horiba). The samples were excited with a 532 nm laser line through an X50 microscope objective. The excitation power was maintained low (10% of the maximum power using OD filters) to ensure no excessive heating and degradation of the samples. The spectra accuracy was 1 cm^{-1} thanks to an 1800 gr mm^{-1} grating. The content of specific valence ions within the samples was checked using X-ray

photoelectron spectroscopy (XPS). The measurements were performed in a Prevac spectrometer, with a focused monochromatic Al Ka source (1486.6 eV). A pass energy of 20 meV was used for all spectra acquisition but the survey scans for which a pass energy of 40 meV was chosen. Sample charging was partially compensated using a flood gun and by depositing the nanocrystals on a conductive Cu tape. Accordingly, the Oα peak was set at 529 eV and the Ce3d signal commonly referred to as v''' was set at 898.4 eV. The background was removed using the Shirley background function and all peaks were fitted with a Voigt shape function.

Transmission Electron Microscopy characterization was carried out with a Thalos F200X instrument (Thermo Fisher) equipped with four Silicon drift detectors (SDD) for Energy Dispersive X-ray spectroscopy (EDX). Concerning TEM sample preparation, the powders were drop-casted onto Cu holey carbon grids after being dispersed and sonicated in isopropyl alcohol. Before insertion into the microscope column, the samples were plasma-cleaned in a 100% Ar atmosphere. For the analysis of TEM and EDX data, Velox software (Thermo Scientific) and Gatan Microscopy Suite (Gatan) were used. The structural model for CeO_2 (cubic, Fm-3m space group) can be found in the Crystallography Open Database (COD ID: 4343161). The size distribution of the nanoparticles was determined by measuring the projected area in high-resolution TEM images with ImageJ software and subsequently calculating the diameter, supposing spherical geometry (analysed nanoparticles up to approximately 100).

2.4 Photocatalytic experiments

Photocatalytic tests were performed in a cylindrical pyrex batch reactor (ID = 2.5 cm; height = 18 cm), irradiated by four lamps emitting light in the visible region (8 W, Philips; emission wavelength in the range 400-700 nm; light intensity incident on the external photoreactor surface: 26 mW/cm^2 [39]) surrounding the photoreactor and placed at the same distance from its external body (at about 30 mm). A cooling fan was placed above the photocatalytic system to prevent the reaction temperature from

exceeding 28 °C. A specific N_2 flow rate (0.250 NL min^{-1}), used as a carrier for the reaction products in the gas phase, was regulated with a mass flow controller (Brooks Instrument). An aqueous solution containing methanol (used as a sacrificial agent [40, 41]) with an initial concentration equal to 10 vol% was used in the photocatalytic hydrogen evolution tests. The total solution volume was 80 mL and a photocatalyst of 1 g L^{-1} was used for the photocatalytic tests. A peristaltic pump (Watson Marlow) ensured continuous mixing of the suspension within the reactor through an external recirculation system. The suspension was left in dark conditions for 60 min. Thereafter, the photocatalytic reaction was initiated under visible light for 240 min. Data acquisition was performed via a gas analyzer (ABB, Advance Optima AO2000) connected to LabVIEW software, enabling the real-time monitoring of H_2 and CO_2 concentration coming from the photoreactor during the irradiation time. Recyclability tests were performed on the photocatalyst that demonstrated the best photocatalytic performance in terms of hydrogen production.

3. Results and Discussion

3.1 Reverse micelle approach

3.1.1 About the synthesis method

Among the different types of wet chemical processes, the reverse micelle approach is particularly effective in controlling the nucleation and growth of nanoparticles (NPs), while improving the extent of doping. This is achieved by channeling reactions that normally occur in aqueous media into the small domains of reverse micelles. The aqueous core of these micelles can be considered an ideal reactor that promotes intimate contact between the precursors, achieving homogeneity and mixing on an atomic scale [42].

Table 1 lists the results of the quantitative ICP-MS analysis of samples prepared by the reverse micelles method. The excellent agreement with the nominal iron contents further extends the features mentioned above to the preservation of defined stoichiometry. Therefore, the samples are subsequently labeled as Fe(x%)-CeO_2 RM, where x% is the nominal Fe amount (molar %).

Table 1: Nominal iron content and chemical composition calculated from ICP-MS elemental analysis

Sample	Nominal composition Fe/(Fe+Ce) (molar %)	Analysed composition Fe/(Fe+Ce) ICP-MS (molar %)
CeO_2 RM	-	-
Fe(1%)-CeO_2 RM	1.0	0.8
Fe(1.5%)-CeO_2 RM	1.5	1.1
Fe(2.5%)-CeO_2 RM	2.5	2.8
Fe(5%)-CeO_2 RM	5	4.2

3.1.2 Characterization results

Fig. 1 shows the diffraction spectra of ceria samples prepared by the reverse micelle method at different iron contents. As can be seen, despite the low heat treatment temperature, the fluorite phase crystallization, typical of cerium oxide, is obtained (JCPDS files 34–0394). In particular, peaks in bare CeO_2 at 28.46°, 32.91°, 47.23°, 56.01°, 69.40°, 76.70°, 79.07° and 88.41° can be associated with planes 111, 200, 220, 311, 400, 311, 420 and 422 respectively. In iron-containing samples, the fluorite-type structure is preserved without any evidence of diffraction peaks belonging to iron phases. Furthermore, the displacement of the diffraction peaks towards higher Bragg angles reveals a decrease in the crystal lattice spacing, proving that iron ions have successfully doped the CeO_2 lattice by isomorphically replacing cerium ions (Fig. SI-1) [24, 43]. As shown in Fig. 1b, the lattice

parameter experiences a constriction with the iron content; in particular, the crystalline lattice constant shows a linear dependence with the dopant concentration following Vegard's law. This behaviour reflects the absence of secondary phases [44]. The crystallite size obtained by applying Scherrer's formula indicates that precipitation in the confined space generated by inverse micelles is particularly effective in generating ultra-small nanocrystals, around 4.0 nm, without significant differences with iron content, Table 2. This means that the obtained nanoparticles show a quantum confinement effect, being the particle size less than the Bohr radius, which for CeO_2 is 7-9 nm [45].

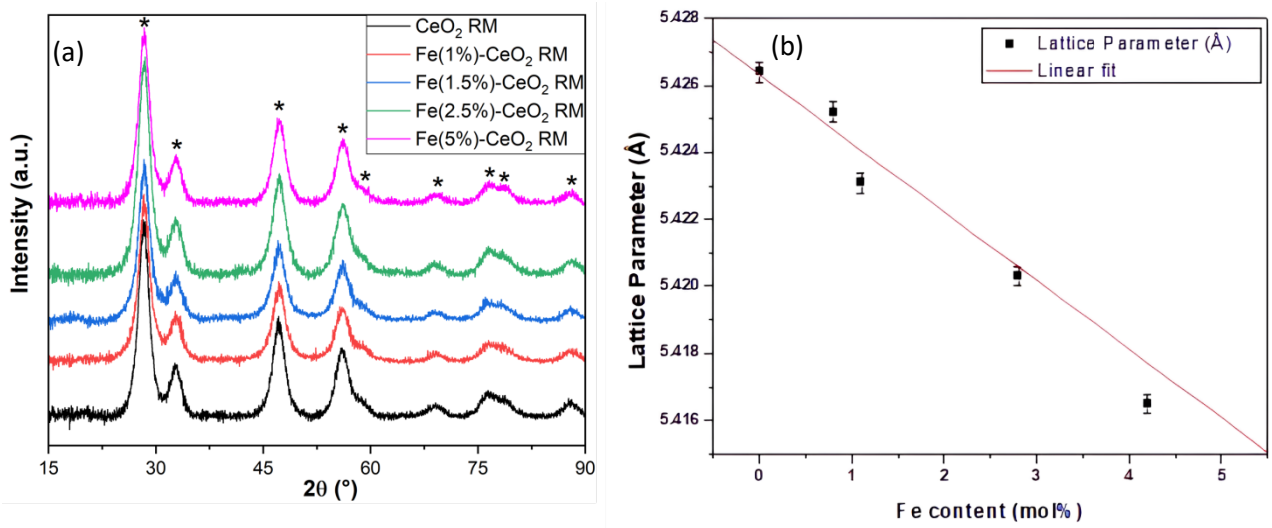

Fig. 1. (a) XRD patterns of the catalysts prepared by reverse micelle at different iron content. The fluorite phase of cubic cerium oxide, CeO_2, is indicated with the asterisk symbol (JCPDS card numb. 34–0394), (b) Vegard's law: cell parameter (Å) of Fe(x%)-CeO_2 RM samples versus iron content measured by ICP-MS

The UV-Vis absorption spectra of the RM samples are shown in Fig. 2a. Three contributions can be distinguished in all profiles, at 214 nm, 270 and 340 nm. The peak at about 270 nm, which corresponds to an energy value of 4.6 eV, was attributed to the energy gap between the occupied O2p and unoccupied Ce4f levels. The assignment of the band at 214 nm is more debated, Liu et al. [46] associated it with charge transfer transitions of $Ce^{3+} \leftarrow O^{2-}$ while Balestrieri et al. [47] interpreted the

high-energy absorption band (around 5.8 eV) as a combination of the charge transfer of the localized 4f electrons of Ce^{3+} to the conduction band of Ce5d and the charge transfer O2p →Ce5d (above 5.5 eV). The absorption at 340 nm can instead be attributed to interband transitions, although some authors relate it to quantum confinement effects due to the particle size, smaller than the Bohr radius of the ceria. In all samples, the optical absorption region extends well below the typical absorption edge of CeO_2. The optical band gaps (Eg) of the prepared and calcined CeO_2 nanoparticles can be estimated using Tauc's relation plotting (F(R)(hν)^1/2) as a function of the photon energy, hν, Fig. 2b. Indirect Eg values obtained by the double tangent method, Table 2, show a gradual decrease with iron content, proving the effectiveness of ceria doping. Yang et al. stated that one of the main reasons for the enhanced visible-light photocatalytic activity of iron-doped ceria samples lies in the downward movement of the CB with a consequent decrease in the band gap [29].

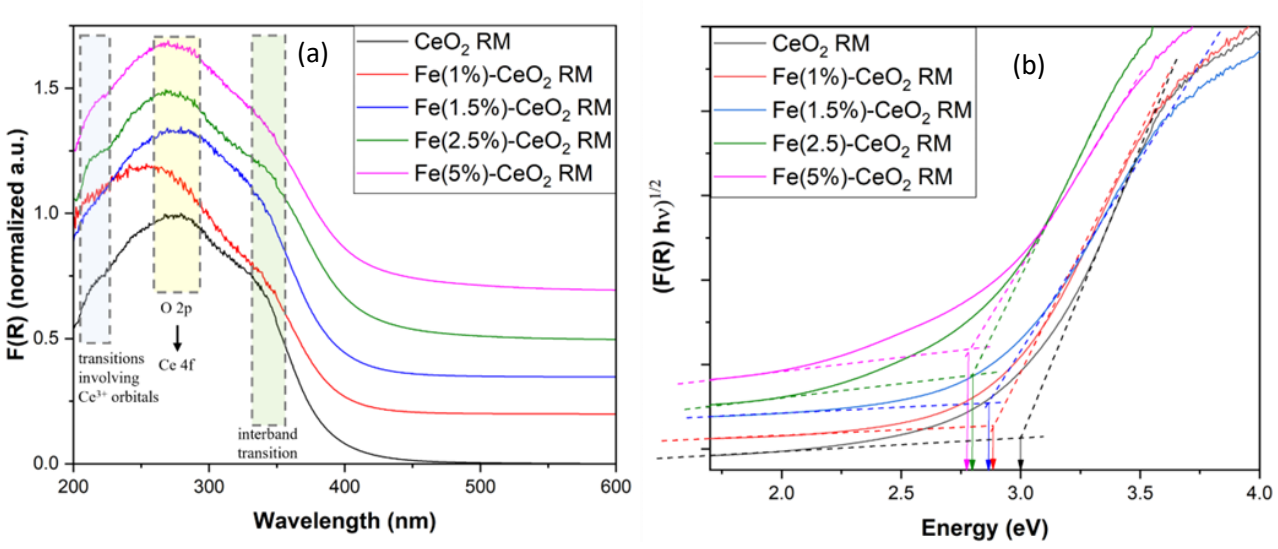

Fig. 2. (a) DR UV-Vis spectra plotted as Kubelka- Munk function F(R) for CeO_2 RM and Fe(x%)-CeO_2 RM samples. (b) The indirect band gap calculation of CeO_2 RM and Fe(x%)-CeO_2 RM samples based on the Kubelka-Munk function by Tauc plot relation using the double tan approximation

Table 2. Summary of structural, optical and textural data of Fe(x%)-CeO_2 RM samples

Sample	Crystallite size [nm][a]	Band gap [eV]	SSA_{BET} [$m^2 g^{-1}$]	Total Pore Volume [$cm^3 g^{-1}$]
CeO_2 RM	4.3	3.00	142	0.182
Fe(1%)- CeO_2 RM	4.3	2.88	140	0.139
Fe(1.5%)- CeO_2 RM	4.2	2.87	143	0.134
Fe(2.5%)- CeO_2 RM	4.0	2.79	163	0.153
Fe(5%)- CeO_2 RM	4.2	2.77	148	0.122

[a] Calculated using the Scherrer equation for (111) plane

Photoluminescence spectroscopy is a non-destructive optical method that can provide information on the electronic structure of materials. In particular, it is possible to follow the fate of the electron-hole pair through the emission spectra obtained for a defined excitation λ. Fig. 3 shows the emission spectra of samples prepared by the reverse micelle method, bare ceria and iron-doped ceria in different percentages. To assign peaks in the spectra to specific transitions, it is necessary to map the energy diagram of the ceria electronic band structure. Regarding the latter, the valence band (VB) is formed by O2p orbitals while the conduction band (CB) by Ce5d orbitals, resulting in a band separation of 6 eV. The band gap is then lowered to about 4.5 eV by the presence of the narrow sub-band generated by the empty orbitals of the $Ce^{4+}4f^0$ states [29, 48]. [The diagram is further complicated by the observation that the cerium oxide, CeO_2, is rarely stoichiometric, leading to the crowding of energy states generated by the numerous imperfections present both in the core and on the surface of the nanoparticles. These intrinsic defects in ceria are highly dependent on the synthesis method [49]. Entering into the details, the presence of a certain fraction of Ce^{3+} ions in the solid causes a sub-band at 1.3-1.5 eV above VB, while the states related to oxygen vacancies, the most important defects in ceria nanocrystals, lie below $Ce^{4+}4f^0$ and are involved in visible emissions [48]. These are commonly referred to as F^0, F^+ and F^{++} depending on whether they contain 2, 1, or 0 electrons, respectively. Besides these, F^0*, F^+*, which are empty excited energy states and are close to the CB, fill out the band structure [29, 48]. Based on this sequence of energy states, we can attribute the peak at 402 nm

to CB → VB emission, 425 nm (violet) to the F^{++} $Ce^{3+}4f^{1}$ transition, 488 nm (green-blue) to F^{+}*→ F+ and 518 nm (green) to F^{0}* → F^{0} emissions. Replacing Ce^{4+} with a cation possessing a lower ionic charge, such as Fe^{3+}, generates an increase in oxygen vacancies and further promotes Ce^{4+} to Ce^{3+} conversion. As a result, defective states increase, also giving rise to non-radiative decay processes. From Fig. 3, it can be seen that the photoluminescence signal and the contribution of the individual colors decrease as the iron content increases, with a maximum for sample Fe(2.5%)-CeO_2 RM to which the greater charge delocalization can be attributed.

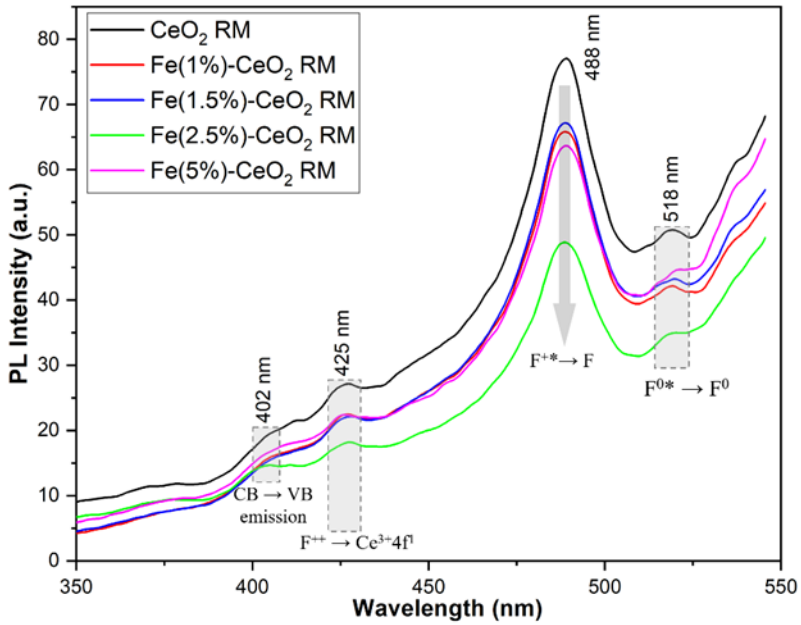

Fig. 3. Photoluminescence spectra of CeO_2 RM and Fe(x%)-CeO_2 RM samples

The specific surface area and features of the porous network were obtained by N_2 adsorption at low temperatures (-196 °C). The adsorption/desorption isotherms, Fig. 4a, resemble type IV, typical of mesoporous materials, with an H2(a) hysteresis loop characterized by a steep branch of desorption, which can be attributed to either pore blocking/percolation in a narrow pore interval or cavitation-induced evaporation. Moreover, the H2-type hysteresis loop is typical of inkbottle mesopores [50]. The abrupt increase at the end of adsorption is associated with the start of bulk condensation of the

adsorbing gas to liquid [51]. The specific BET surface areas, Table 2, show consistently higher values than those obtained by conventional precipitation method, *vide infra*.

The BJH method on desorption branches was used to obtain the pore size distribution (PSD), Fig. 4b. The distributions are rather narrow, centered at values around 3.6 nm, showing that the reverse micelle method is effective in the preparation of mesoporous ceria and doped ceria. it is worth pointing out that the PSD curve is slightly shifted towards higher values for sample Fe(2.5%)-CeO_2 RM.

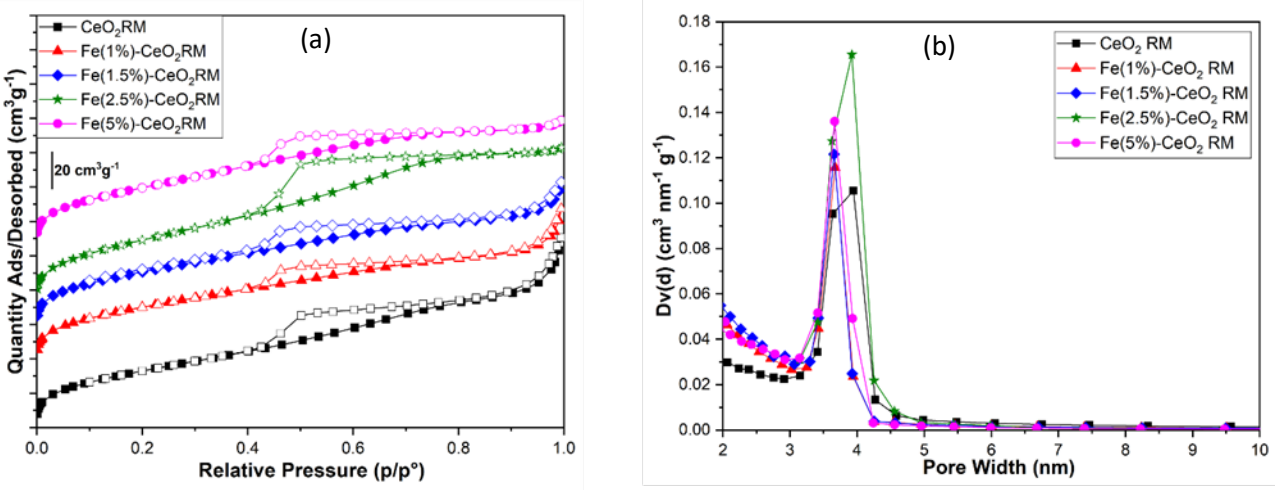

Fig. 4. (a) N_2 adsorption/desorption isotherms at -196 °C of CeO_2 RM and Fe(x%)-CeO_2 RM samples. The curves are shifted for the sake of clarity. Adsorption and desorption branches were indicated with filled and empty symbols, respectively. (b) BJH pore size distribution (PSD) plot obtained from the desorption branch of the isotherm for CeO_2 RM and iron-doped samples**.**

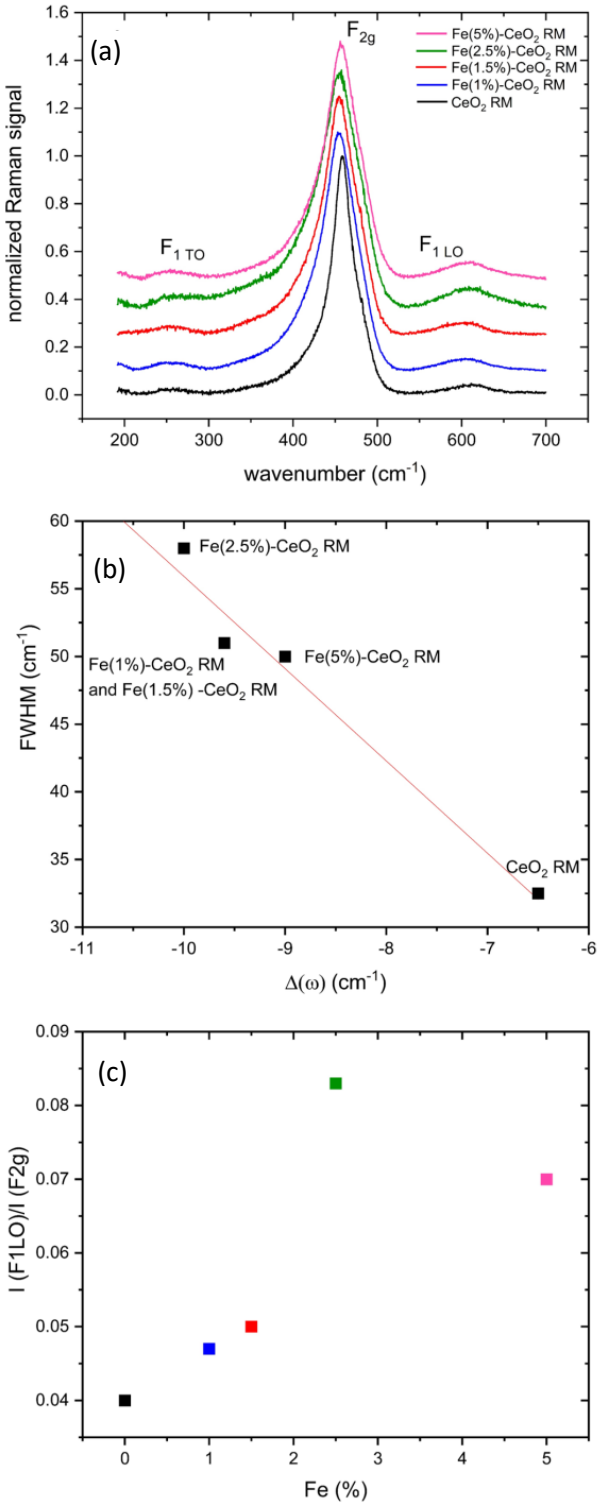

Fig. 5. (a) Raman spectra of CeO_2 RM and Fe(x%)-CeO_2 RM samples. (b) variation of the Raman line broadening (FWHM) of the F_{2g} peak of CeO_2 RM and Fe(x%)-CeO_2 RM samples as a function of the peak position shift Δω (as referred to pristine CeO_2). (c) Variation of the F_{1LO}/F_{2g} intensity ratio of CeO_2 RM and Fe(x%)-CeO_2 RM samples as a function of Fe content.

Fig. 5a presents the Raman, spectra of all doped and undoped CeO_2 RM samples. Three peaks can be distinguished. The prominent peak at 458.5 cm^{-1} is the F_{2g} peak, related to the vibration of the O sublattice. Both its position and full-width-at-half-maximum (FWHM) depend on the Fe content. As previously reported by Popovic et al. [52] and our group [24], their correlated linear variation, as presented in Fig. 5b, is indicative of the charge delocalization of the 4f electrons located at Ce(Fe)-VO-Ce(Fe) centers. It is worth mentioning that the variation also depends on the size and strain of the nanocrystals. Since neither the size nor the strain varies within our sample (according to XRD analysis), we can estimate that this linear variation is thus evidence of the oxygen deficiency and therefore of the doping efficiency. Consequently, the most efficient doping is obtained with a content of 2.5% of iron.

Still, in Fig. 5a, the F_{1TO} and F_{1LO} peaks appear at 270 cm^{-1} and 606 cm^{-1} respectively. Forbidden in pristine CeO_2, they appear in defective ceria due to long-range symmetry breaking. In particular, the F_{1LO} peak is related to the presence of oxygen vacancies. In Fig. 5c, we plot the intensity variation of the F_{1LO} peak normalized to the F_{2g} peak intensity compared to the Fe content. Consistently, the most oxygen-deficient sample is Fe(2.5%)-CeO_2 RM, indicating the highest doping efficiency at 2.5% Fe content. As extensively presented in the literature, the presence of oxygen vacancies can lead to increased photo-oxidation performance as they constitute trapping centers for photogenerated electrons, effectively limiting the rate of electron-hole recombination [53, 54]. Substitutional doping with the formation of oxygen vacancies, one oxygen vacancy coupled with two M^{3+} for charge neutrality, can be considered a dominant mechanism up to a certain iron content. However, it is worth mentioning that the small size of the Fe^{3+} also allows for an interstitial dopant compensation mechanism, in which three Fe^{3+} in the substitution sites are coupled to one in the interstitial sites. The latter mechanism leads to a decrease in oxygen vacancy concentration, and this is what most probably happens in the 5% iron sample [55].

The efficiency of Fe introduction in the lattice to promote a change of the Ce ions valence, and thus the creation of VO, can be probed with XPS. The Ce3d spectrum, shown in Fig. SI-2, consists of five

$3d_{5/2}$ components, labeled v_0 (880.6 eV), v (882.6 eV), v' (885.4 eV), v'' (888.8 eV) and v''' (898.4 eV) as well as the five 3d3/2 components, labeled u_x, separated by 18.45 eV from the previous ones, with a fixed ratio u_x/v_x of 1.5. More specifically, the areas of the v_0, u_0, v' and u' features are used to quantify the concentration of surface Ce^{3+} ions. The result is plotted in Fig. 6. Several authors [56, 57] have highlighted that such quantification has to be taken with caution since XPS probes only a few nm below the surface of the nanocrystals and also because the ceria surface is sensitive to X-rays. In other words, the X-ray probe can alter the valence state of the surface Ce ions. To avoid as much as possible any artifact in the analysis, we analyzed the spectra in the same way. This means that the irradiation time required to set the spectrometer parameters was identical to all samples so that the possible modification of the samples under the beam, if any, were identical too. This does not allow an absolute quantification of Ce^{3+} concentration but it does allow a relative quantification and thus the comparison from sample to sample. The relative variation in Fig. 6 clearly shows that for Fe content increasing from 0 to 1% the Ce^{3+} increases while it further decreases as the Fe content exceeds 1%.

Three components are usually considered to resolve XPS spectra of the O1s core level in CeO_2 (as shown in Fig. SI-3). The first one, labeled Oα at 529 eV, is usually associated with lattice oxygen, i.e. Ce^{4+} in CeO_2. According to [58], the Oβ feature at 531 eV and Oγ feature at 532 eV can be attributed to surface hydroxyl groups, resulting from the dissociation of adsorbed water and irreversibly adsorbed molecular water, respectively. Interestingly, the fraction of the Oγ feature follows the same trend as that of the Ce^{3+} (see Fig. 6). This proves that, as stated by Idriss et al. [58], the Oγ characteristic cannot be a direct signature of the creation of oxygen vacancies. It rather reveals that the irreversible adsorption of molecular oxygen depends on the presence of Ce^{3+} at or close to the surface. Importantly for H_2 production or any surface reaction, it is necessary to have the Oγ feature low as this feature is the signature of surface sites that are irreversibly occupied and thus no longer available for reactions.

Based on the XPS observations, we can propose the following scenario regarding the effect of Fe incorporation. For a low content of Fe (below 1%), its incorporation as Fe^{3+} into the network induces the reduction of Ce^{4+} to Ce^{3+}. This reduction is accompanied by the creation of VO for the sake of charge compensation. When the Fe content exceeds 1%, this process is no longer valid. Instead, we can imagine that two Fe^{3+} ions directly replace two Ce^{4+} ions, without the reduction to Ce^{3+}, with the creation of VO. This accounts for the non-linearity between the increase in iron content and the increase in Ce^{3+}. The surface VO can serve as the reactive sites and trap the separated charge carriers for the subsequent quick surface reaction [59]. However, to achieve a delayed recombination pathway via oxygen vacancies, the right concentration and distribution of VOs must be obtained to favour the performance of a semiconductive photocatalyst. The generation of VO cannot, however, be traced through gamma oxygens because, as already mentioned, they are related to the irreversible adsorption of molecular oxygen and are detrimental to photocatalytic activity. In conclusion, iron does not in itself add active sites in the ceria but changes its structure, creating defects that are strictly dependent on its content.

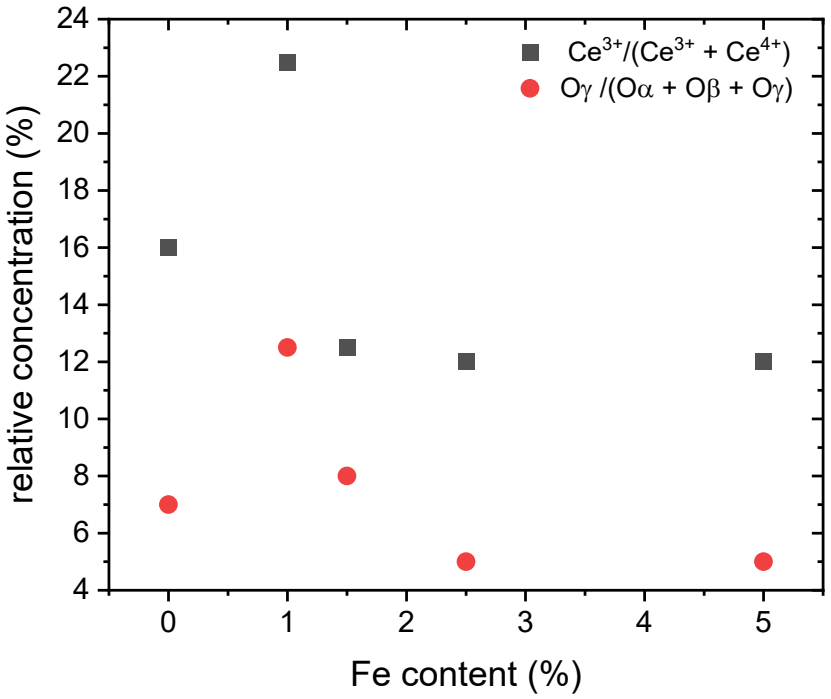

Fig. 6. Evolution of the Ce^{3+} relative concentration and Oγ relative concentration as a function of Fe content in the Fe(x%)-CeO_2 RM nanocrystals

3.1.3 Visible-light driven hydrogen evolution using Fe(x%)-CeO_2 RM photocatalysts

The photocatalytic hydrogen evolution during the irradiation time under visible light was evaluated for all the photocatalysts prepared with the reverse micelle method using a photocatalyst dosage of 1g L^{-1}.

Before the photocatalytic tests, blank experiments were carried out by irradiating the methanol solution without photocatalysts. The results evidenced no appreciable amount of evolved hydrogen, indicating that the latter was produced from the methanol solution only by photocatalytic reaction.

Fig. 7 reports the hydrogen production (μmol of H_2 evolved in the gaseous phase with respect to the volume in L of methanol aqueous solution) achieved in the presence of Fe(x%)-CeO_2 RM and CeO_2 RM photocatalysts.

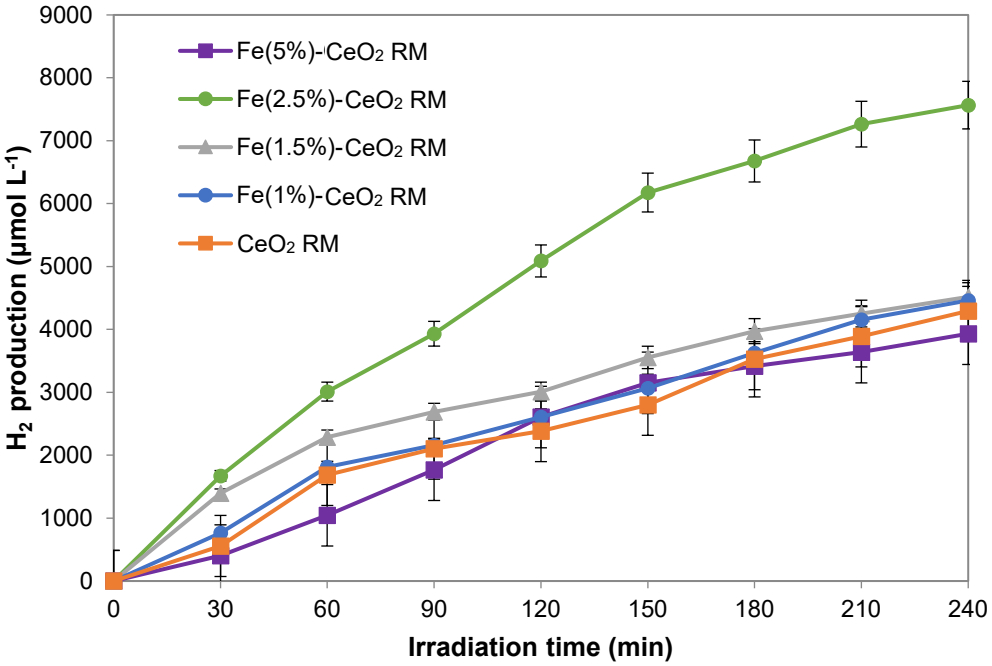

Fig. 7. Hydrogen evolution under visible light for CeO_2 RM and Fe(x%)-CeO_2 RM photocatalysts.

A gradual increase in hydrogen production as a function of irradiation time was observed for all the tested photocatalysts. In detail, CeO_2 RM showed a hydrogen production of about 4290 µmol L^{-1} after 240 min of reaction time. The photoactivity of the CeO_2 RM sample under visible light could be explained by considering the physicochemical characterization results. Specifically, PL spectrum, XPS and Raman analysis of the CeO_2 RM evidenced the presence of electronic transitions due to Ce^{3+} ions and oxygen vacancies in the ceria fluorite nanocrystals, which can promote the visible light activity of pure CeO_2 samples, as shown in the literature [60, 61]. It is reported that the presence of intrinsic defects (such as Ce^{3+} and oxygen vacancies) in the ceria crystalline structure generates intermediate energy levels between VB and CB, inducing the lowering of the band gap energy value with respect to that observed for a commercial CeO_2 sample (about 3.2 eV [62], see Fig. SI-4). Indeed, the UV-Vis results (Fig. 2) evidenced an absorption onset for CeO_2 RM at about 413 nm, corresponding to a band gap of 3 eV (Table 2), justifying the observed activity of this photocatalyst under visible light (Fig. 7).

The experimental data reported in Fig. 7 also allow us to assess the effect of Fe load on photocatalytic performances. It is possible to observe that the hydrogen evolution under visible light irradiation with Fe(x%)-CeO_2 RM photocatalysts was higher than that of CeO_2 RM when the Fe doping amount was increased from 1 to 2.5 mol%. The further increase of the dopant level from 2.5 to 5 mol% was reflected in a decrease in hydrogen production efficiency, reaching a value lower than pure CeO_2. In detail, the hydrogen evolution value after 240 min of irradiation time for Fe-CeO_2 RM, Fe(1%)-CeO_2 RM, Fe(1.5%)-CeO_2 RM, Fe(2.5%)-CeO_2 RM and Fe(5%)-CeO_2 RM were 4290, 4460, 4520, 7566 and 3930 μmol L^{-1}, respectively. It is well known that the improvement of photocatalytic performance under visible light for doped semiconductors is attributed to the synergistic effect of different parameters, such as oxygen vacancies, photocatalyst crystal size reduction, band gap value reduction and suppression of the recombination rate of electron-hole pairs [63].

Moreover, in the case of Fe-doped CeO_2 photocatalysts, the literature findings evidence that the presence of Fe^{+3} ions in the CeO_2 lattice act as electrons acceptor (reducing Fe^{+3} to Fe^{2+}) and/or positive holes donor (oxidizing Fe^{3+} to Fe^{4+}), thus extending the average life of the charge carriers (i.e reduction of their recombination phenomena) [64, 65].

Based on our data on photocatalytic activity (Fig. 7) and physicochemical characterization of Fe(x%)-CeO_2 RM photocatalysts, we tried to explain the trend of hydrogen photoproduction with the iron content in the CeO_2 lattice. To this purpose, the hydrogen evolution values after 240 min of irradiation time were plotted as a function of the band gap values (Fig. SI-5), the SSA_{BET} (Fig. SI-6) and the reduction percentage of the PL signal (with respect to that of CeO_2 RM) detected at 487 nm (Fig. SI-7) for Fe(x%)-CeO_2 RM photocatalysts. Interestingly, no clear correlation was found, which indicates that photocatalytic hydrogen production performance under visible light cannot be linked to the above parameters taken individually. On the other hand, the activity of a photocatalyst in visible light is undoubtedly a complex interaction of several interdependent factors. It was also reported that the catalyst pore volume can play an important role in tuning the photoactivity [66-69]. More specifically, it has been argued that a higher pore volume of the photocatalyst favors the diffusion phenomena of

the reactants toward the active sites, resulting in higher photocatalytic activity [70]. Based on this observation, we decided to normalize the hydrogen detected in the gas phase with respect to the total pore volume of the Fe(x%)-CeO_2 RM photocatalysts (Table 2) and to analyze its trend as a function of the reduction percentage of the PL signal at 487 nm (Fig. 8).

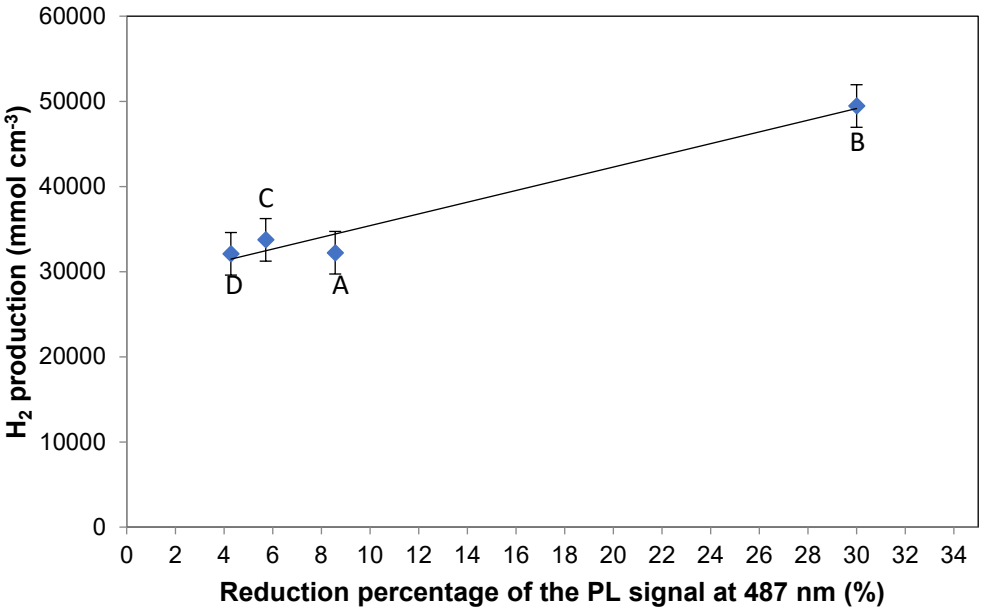

Fig. 8. Hydrogen production after 240 min of irradiation time normalized with respect to the total pore volume of Fe(x%)-CeO_2 RM photocatalysts as a function of the reduction percentage of PL signal at 487 nm. A, B, C and D are referred to Fe(5%)-CeO_2 RM, Fe(2.5%)-CeO_2 RM, Fe(1.5%)-CeO_2 RM and Fe(1%)-CeO_2 RM, respectively.

It is possible to observe that, in this case, a good linear correlation was found. Accordingly, we can state that the key features of the Fe(x%)-CeO_2 RM photocatalysts for the photocatalytic evolution of hydrogen under visible light are the ability to reduce the recombination rate of electron-hole pairs and an adequate total pore volume, together with an appropriate band gap value. On the other hand, these characteristics mirror the structural, optical and textural characteristics, which are highly dependent on the type of synthesis and the dopant loading. Indeed, the highest hydrogen production (7566 μmol L^{-1}) was achieved in the presence of Fe(2.5%)-CeO_2 RM photocatalyst that, among the Fe(x%)-CeO_2 RM samples, evidenced the lowest intensity of PL signals (Fig. 3) and the highest total pore volume

(Table 2). Instead, the lowest hydrogen production (3930 μmol L^{-1}) was observed in the presence of Fe(5%)-CeO_2 RM photocatalyst that, in turn, was characterized by PL signals at a higher intensity and by the lowest total pore volume. These results are also consistent with literature papers in which it is evidenced that the increase of the dopant element load in the host lattice beyond the optimal value (i.e in our case from 2.5 to 5 mol % in CeO_2 lattice) leads to a decrease in the photocatalytic activity under visible since the excess dopant content would act as a recombination center for photogenerated electron-hole pairs [19, 24, 71, 72]. In summary, an iron content of 2.5 mol% seems to be the optimal value for the CeO_2 doping by reverse micelle route since the Fe(2.5%)-CeO_2 RM photocatalyst showed the highest hydrogen production under visible light irradiation.

To check the Fe(2.5%)-CeO_2 RM stability under the used operating conditions, the photocatalytic experiments were repeated for six reuse cycles. In particular, the suspension was removed from the reactor after each reuse cycle, and centrifuged to remove the photocatalyst particles, which were then dried at room temperature for 48 h to be reused in the next reuse test. The obtained results are reported in Fig. 9.

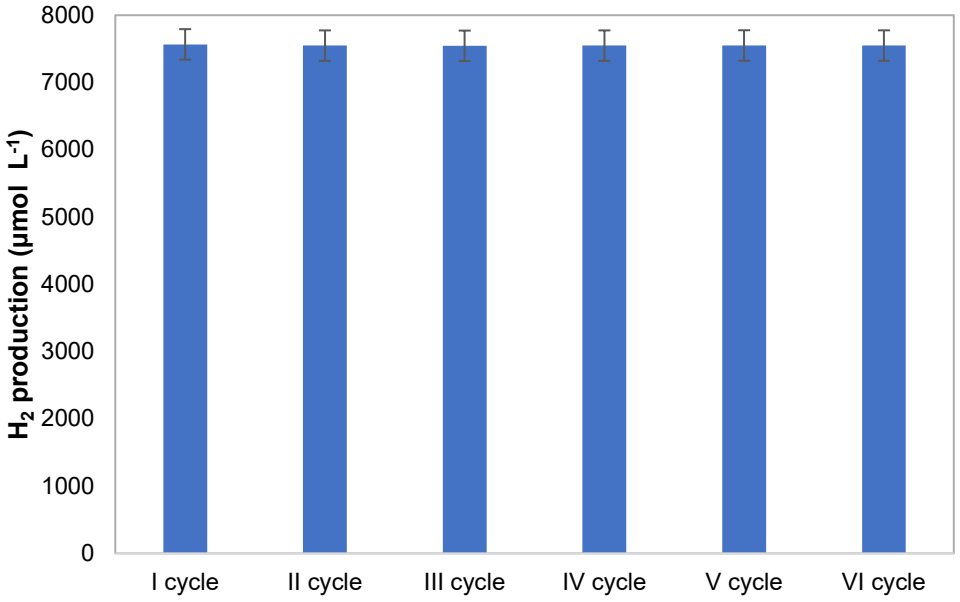

Fig. 9. Hydrogen production after 240 min of visible light using Fe(2.5%)-CeO_2 RM for six reuse cycles.

Interestingly, photocatalytic hydrogen production did not change significantly, confirming the high stability of the optimal photocatalyst. To further assess the stability of the Fe(2.5%)-CeO_2 RM catalyst, a comparison of the structural and optical properties before and after six reuse cycles was conducted (Fig. SI-8). The XRD diffraction pattern of the Fe(2.5%)-CeO2 RM_spent catalyst (Fig. SI-8a) shows the presence of the fluorite phase without any significant distortion of the structure. Concerning the optical properties, the UV-Vis and photoluminescence spectra of the post-reaction catalyst also exactly resemble those of the fresh catalyst (Figs SI-8b and SI-8c). These comparisons strongly support the stability of the catalyst.

3.2 Impact of the preparation method for Fe-doped CeO_2 on photocatalytic hydrogen evolution under visible light

3.2.1 Conventional precipitation

To highlight the advantages of the reverse micelle method, the best catalyst, with an iron content of 2.5 %, and bare ceria were also prepared by simple co-precipitation. The latter method is widely used to prepare mixed oxides for the sake of simplicity of the experimental setup, low cost, and the absence of organic solvents [73]. In the co-precipitation reaction, hydroxides are obtained by adding a certain volume of ammonia to an aqueous solution of the metal salts. The filtered and washed co-precipitate is heat-treated at the same temperature as the catalysts prepared for inverse micelles. The most critical aspect of this method, which makes it not very versatile, concerns the degree of homogeneity of the system and the little control over particle size and distribution as evidenced by the following characterization.

3.2.2 Characterization

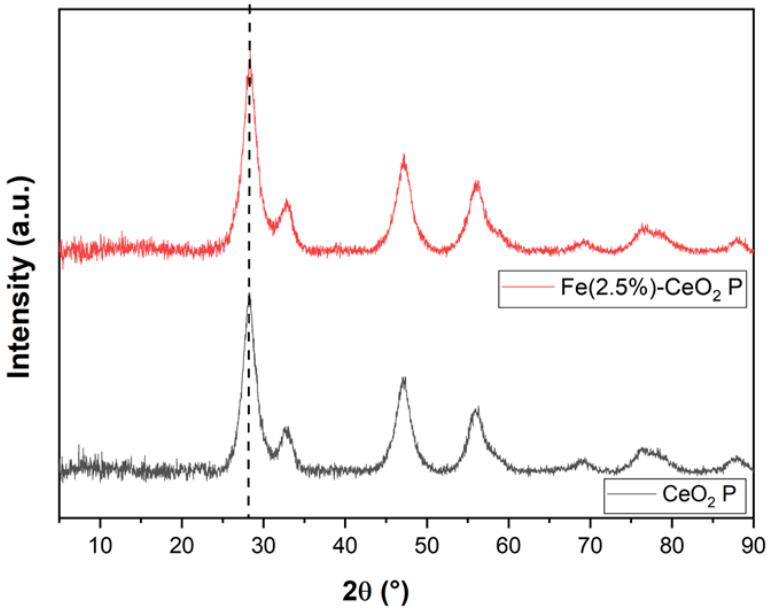

Fig. 10. XRD patterns of the CeO_2 P and Fe(2.5%)-CeO_2 P photocatalysts

Differently from what was observed with reverse micelles, the shift in the diffraction lines as the iron content changes is hardly detectable (Fig. 10). This is confirmed by the comparable values of the cell parameter between pure and iron-loaded ceria (Table 3). This result is the first indication that isomorphic substitution of Ce^{4+} by Fe^{3+}, if any, occurs to a negligible extent. Moreover, as can be seen from Table 3, the precipitation method is less effective in guaranteeing an actual composition consistent with the nominal one.

Table 3. Summary of compositional, structural, optical and textural data of CeO_2 P and Fe(2.5%)-CeO_2 P

Sample	Fe/(Fe+Ce) (from ICP-MS) [molar %]	Lattice Parameter [Å][a]	Band gap [eV]	SSA_{BET} [m^2g^{-1}]	Total Pore Volume [cm^3g^{-1}]
CeO_2 P	-	$5.4457 \pm 3x10^{-4}$	2.95	79	0.047
Fe(2.5%)- CeO_2 P	1.5	$5.4451 \pm 3x10^{-4}$	2.92	55	0.035

[a] for fluorite phase, obtained from the cell refinement of the XRD patterns

The UV-Vis absorption spectra of Fe(x%)-CeO_2P samples (Fig. SI-9) show the same profiles, with the three characteristic bands, as the samples prepared with micelles. A noticeable difference is in the inter-band transition, which is more pronounced in Fe(x%)-CeO_2P samples. Katta et al. [74] reported that the intensity of the interband transition increases with increasing particle size, accompanied by a decrease in peak width. This result is in agreement with the presence of larger particles as evidenced by TEM *(vide infra)*. Further evidence of the lower degree of doping obtained by simple co-precipitation in an aqueous medium comes from the Eg values extrapolated from the Tauc diagram (Fig. 11a). These show a slight decrease from CeO_2 to Fe(2.5%)-CeO_2 P.

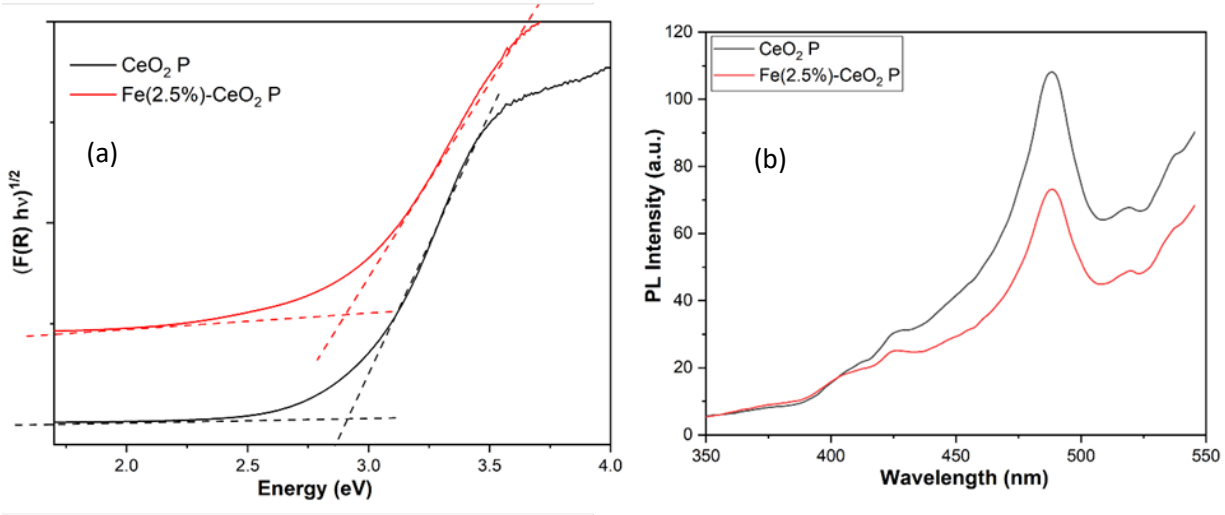

Fig. 11. (a) The indirect band gap calculation of CeO_2 P and Fe(2.5%)-CeO_2 P photocatalysts by Tauc plot relation. (b) Photoluminescence spectra of CeO_2 P and Fe(2.5%)-CeO_2 P photocatalysts

The photoluminescence spectra, shown in Fig. 11b, resemble those obtained for RM samples, with a decrease in PL signal induced by iron loading. Careful analysis reveals, however, that the PL intensities recorded for the P samples are higher than those prepared by the reverse micelle approach, suggesting a faster recombination rate of the charge carriers.

The formation of iron-doped ceria in an aqueous medium, in the absence of confined spaces, negatively affects textural properties. In Fig. SI-10a the adsorption/desorption isotherms show a more

stepwise increase in the volume of adsorbed nitrogen and a more limited hysteresis loop. This is explained by the increase in the number of routes connecting the pores, due to a connectivity dependency of the hysteresis area [75]. The hysteresis can be considered a type II with the lower limit of the desorption branch located approximately at the cavitation-induced p/p° value. The hysteresis loop, classifiable as H4, suggests a different porosity to the RM samples, determined by non-rigid aggregates of plate-like particles. The volumes of adsorbed nitrogen are significantly lower for the Fe(2.5%)-CeO_2 P samples and the textual features, shown in Table 3, reveal values of specific surface area and total pore volume that are significantly lower than those of RM samples. From the pore size distribution, Fig. SI-10b, it is possible to observe the presence of a fraction of small mesopores at the boundary of the micropore characteristic area. Furthermore, the peak centered at 3.6 nm is less prominent than that displayed by the RM samples.

Fig. 12 provides further information on the morphological and structural properties of the RM and P samples, obtained by Transmission Electron Microscopy. Based on high-resolution images (Fig. 12 a, b, c, d) and electron diffraction patterns (Fig. 12e), all the samples are constituted by crystalline nanoparticles, sharing the same CeO_2 cubic structure. Electron diffraction data corroborates the absence of secondary crystalline phases, in agreement with XRD characterization. EDX spectra (Fig. 12f) qualitatively confirm the chemical composition of the RM and P samples, showing the family of characteristic Ce-L lines, alongside a “shoulder” at approximately 6.4 keV corresponding to the Fe-K contribution for the Fe(2.5%) samples. While no significant changes in the crystalline structure are noticed, it is interesting to calculate morphological descriptors for the single nanoparticles directly from the TEM images.

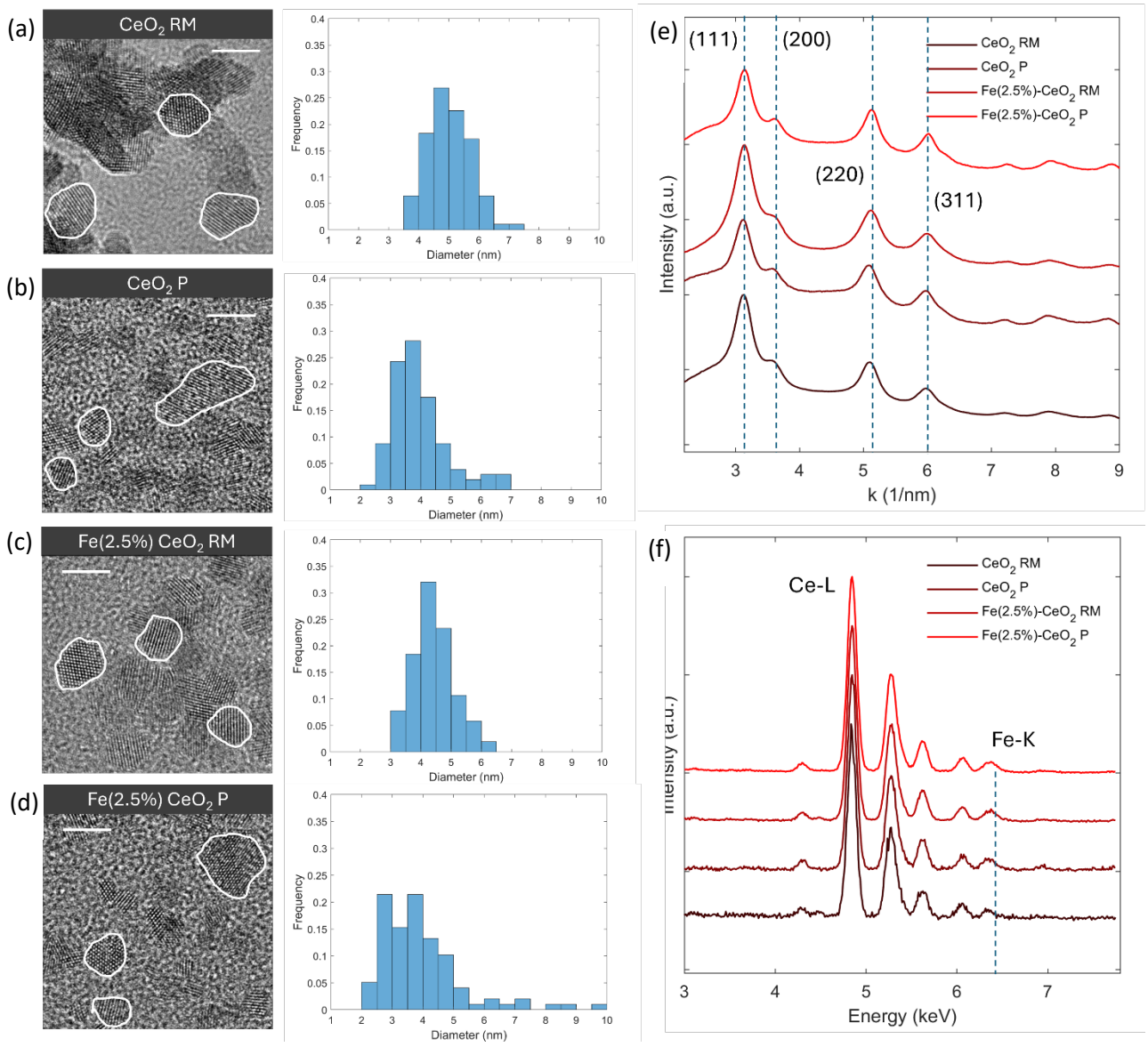

Fig.12. Representative high-resolution TEM images for samples (a) CeO_2 RM, (b) CeO_2 P, (c) Fe(2.5%)-CeO_2 RM, (d) Fe(2.5%)-CeO_2 P, alongside the calculated size distribution of the nanoparticles. The scale bar is 5 nm. Panel (e) provides the rotationally-averaged electron diffraction patterns and (f) the EDX spectra for all the samples.

Fig. 12 shows the distribution in size of the catalysts obtained with the reverse micelle and co-precipitation approaches. First of all, it is interesting to notice that the size distributions obtained directly from the TEM images show a good correlation with the estimated crystallite size values obtained by applying Scheerer's formula on XRD data (~ 4 nm). The catalysts obtained with the

reverse micelle approach show almost monomodal size distribution, with distribution maxima occurring at size ≤ 5nm. Samples obtained with the co-precipitation method exhibit a more scattered size distribution, especially considering Fe(2.5%)-CeO_2 P, with non-negligible contributions in the 6 nm – 9 nm range. Through a careful analysis of HRTEM images (see Fig.s SI-11 and SI-12), it appears that larger particles in the P samples deviate from the approximately circular morphology of the smaller particles, while still retaining the same cubic CeO_2 crystalline structure. Based on the available data, it is possible that the larger particles, considered as 3D objects, may exhibit a plate-like morphology, which might influence the textural properties by reducing the specific surface area of the P samples through the formation of plate-like aggregates *vide supra* (discussion of textural properties).

3.2.3 Photocatalytic activity results

Fig. 13 shows the comparison between the photocatalysts prepared with the traditional precipitation method (P) and those prepared with the reverse micelle approach (RM). In particular, the comparison was carried out for undoped CeO_2 and CeO_2 doped with Fe (at 2.5 mol %). In detail, the Fe(2.5%)-CeO_2 P sample allowed to obtain a hydrogen production equal to 3192 μmol L^{-1} after 240 min of visible irradiation, while the same sample prepared with the reverse micelle method (Fe(2.5%)-CeO_2 RM) guaranteed significantly higher hydrogen production for the same irradiation time. It is worth noting that the CeO_2 RM photocatalyst also showed superior hydrogen production performance to that of CeO_2 P.

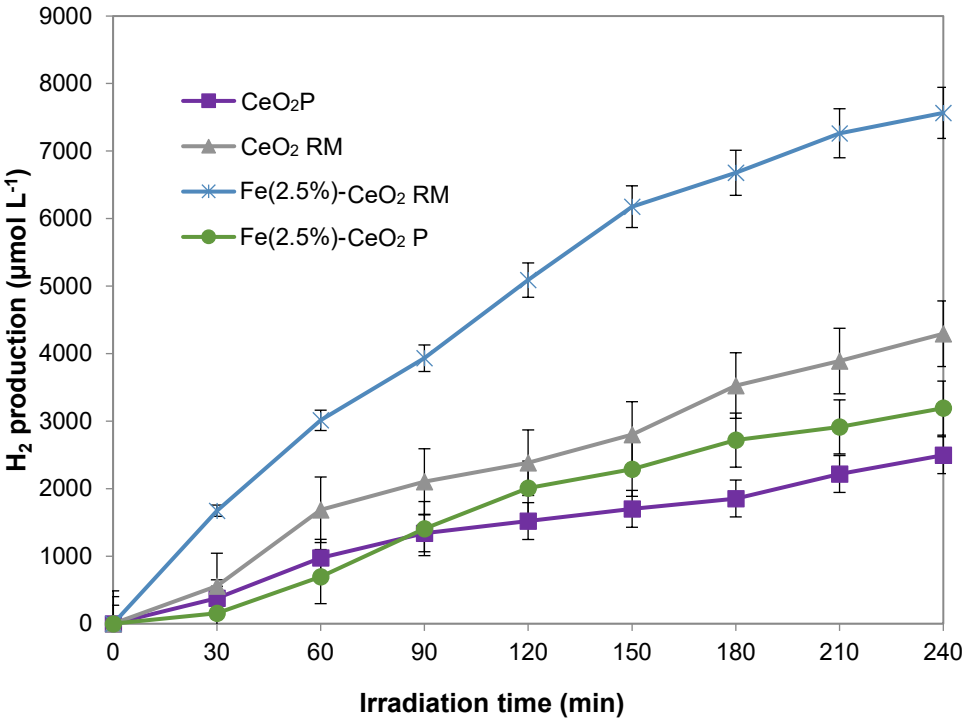

Fig. 13. Hydrogen evolution under visible light for CeO_2 RM, Fe(2.5%)-CeO_2 RM, CeO_2 P and Fe(2.5%)-CeO_2 P photocatalysts.

Several factors could justify the enhanced photocatalytic hydrogen evolution for the Fe(2.5%)-CeO_2 RM with respect to the Fe(2.5%)-CeO_2 P photocatalyst: the increase in S_{BET} value (163 m^2 g^{-1} for Fe(2.5%)-CeO_2 RM vs 55 m^2 g^{-1} for Fe(2.5%)-CeO_2 P) and total pore volume (0.153 cm^3 g^{-1} for Fe(2.5%)-CeO_2 RM vs 0.035 cm^3 g^{-1} for Fe(2.5%)-CeO_2 P), the lowering of band gap energy (2.73 eV for Fe(2.5%)-CeO_2 RM vs 2.93 eV for Fe(2.5%)-CeO_2 P), and the photocatalysts particles morphology and size of the two doped photocatalysts evaluated from TEM analysis (Fig. 12). Furthermore, the enhanced photocatalytic activity for the doped sample prepared via RM approach could also be explained considering that Fe(2.5%)-CeO_2 RM showed PL signals at a lower intensity than those observed for Fe(2.5%)-CeO_2 P (see Fig. 3 and Fig. 11b). This last result is a clear indication that, if compared with the P method, the use of RM approach for the doped photocatalysts preparation can induce extended stability of photogenerated electron-hole pairs (i.e. the decrease in the recombination rate), assuring a longer lifetime of electrons photoinjected and hence an improvement

of photocatalytic hydrogen production. As reported in the literature [76], an extended lifetime of electrons localized in the CB of semiconductors is a key aspect for improving the photocatalytic performance of reactions in which the photogenerated electrons are involved (such as in the photocatalytic hydrogen evolution from aqueous solutions containing a sacrificial agent). Additionally, it is extensively reported that the photocatalyst specific surface area is an important factor for the enhancement of photoactivity because a higher surface area improves the light harvesting on photocatalyst surfaces by increasing the exposed active sites to the light and consequently improving the photocatalytic activity [77, 78]. The S_{BET} value of the Fe(2.5%)-CeO_2 RM photocatalyst is about twice as high as that of the Fe(2.5%)-CeO_2 P sample. This certainly contributed to the significantly improved photoactivity of the doped photocatalyst prepared by the RM method. Overall, based on our experimental results, it was possible to demonstrate the efficiency of the RM approach for the preparation of Fe-doped CeO_2 aimed to boost photocatalytic hydrogen production under visible light.

3.4 Possible reaction mechanism for photocatalytic hydrogen evolution under visible light on Fe(2.5%)-CeO_2 RM photocatalyst

D_2O instead of distilled H_2O was employed during photocatalytic tests to evaluate the role of water in the mechanism for photocatalytic hydrogen evolution under visible light in the presence of Fe(2.5%)-CeO_2 RM photocatalyst. The results obtained with the D_2O+CH_3OH solution compared to that observed with the H_2O+CH_3OH solution are shown in Fig. 14. It is possible to notice that, using D_2O, a significant reduction in hydrogen production was obtained. Indeed, after 240 min of visible light irradiation, the photocatalytic hydrogen production in the presence of D_2O was 3024 μmol L^{-1}, while in the presence of H_2O the hydrogen evolution was higher (7566 μmol L^{-1}). These results indicate that the protons from water molecules were mainly involved as electron acceptors to promote hydrogen evolution. These data agree with the scientific literature papers [79, 80] in which it is

reported that water is the primary source for photocatalytic hydrogen production. On the other hand, the data reported in Fig. 14 evidenced that the amount of produced CO_2 (generated by methanol oxidation pathways) did not change significantly, possibly indicating that methanol was preferentially oxidized by the photogenerated positive holes. Furthermore, the hydrogen production did not decrease to zero with the D_2O+CH_3OH solution, also highlighting that H^+ originating from the oxidation of methanol with the positive holes contributed to the photocatalytic H_2 production reaction, as reported in the literature [81].

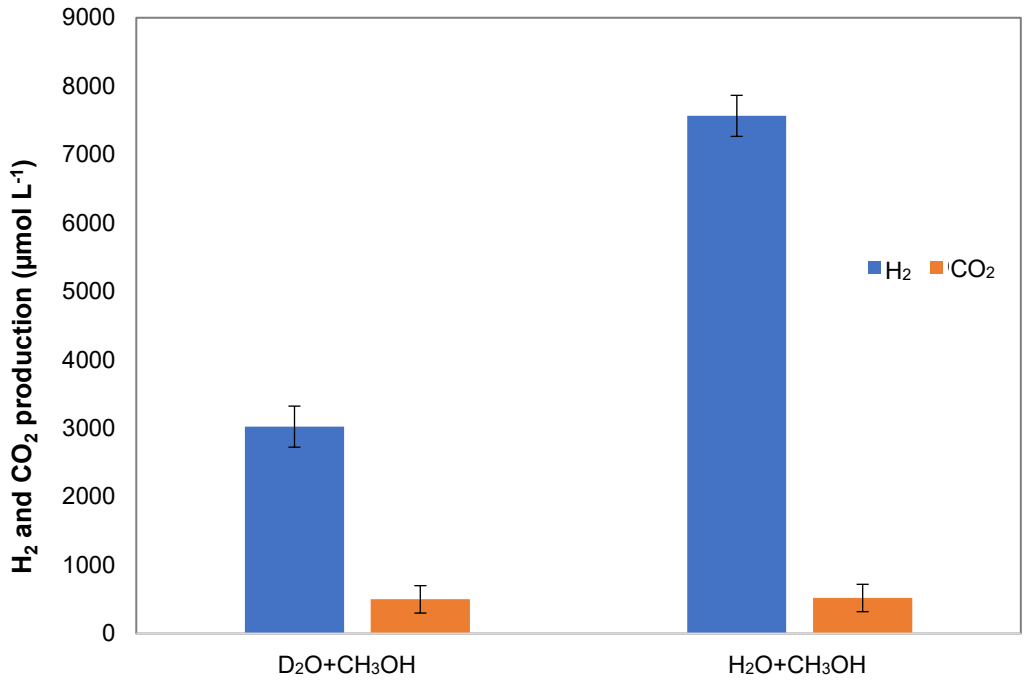

Fig. 14. Photocatalytic hydrogen production after 240 min of visible light using Fe(2.5%)-CeO_2 RM in the presence of CH_3OH/H_2O or CH_3OH/D_2O solution.

It is known that the ability of a photocatalyst to produce hydrogen efficiently is linked to its electronic structure [82]. Considering that the iron content in the Fe(2.5%)-CeO_2 RM photocatalyst is very low (2.5 mol %), it is possible to assume that its electronegativity value is equal to that of pure CeO_2 (5.56 eV) [83]. From the band gap value (E_g) of Fe(2.5%)-CeO_2 RM (2.79 eV), it was calculated the energy

values of CB edge position (E_{VB}) and VB edge position (E_{CB}) at pH=7 through the Mulliken relationship and Nernst equation [84]:

$$E_{VB} = X - 4.5 + (0.5 \times E_g) - 0.059 \times 7$$

$$E_{CB} = E_{VB} - E_g$$

where X is the CeO_2 electronegativity.

The obtained results are schematized in Fig. 15, allowing us to establish the possible visible light-driven photocatalytic mechanism related to the hydrogen evolution in the presence of Fe(2.5%)-CeO_2 RM.

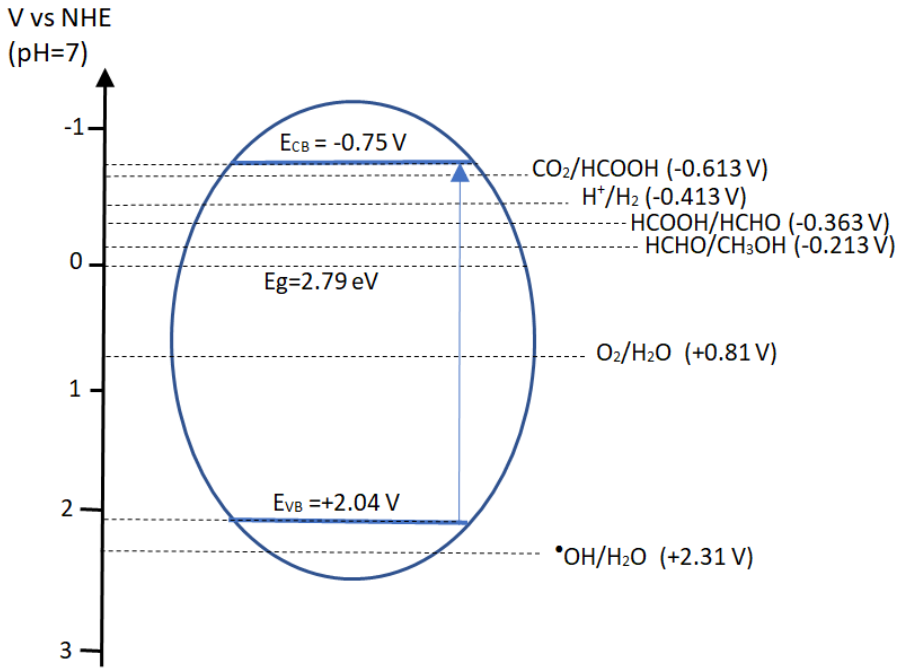

Fig. 15. Schematic diagram of photocatalytic mechanism for hydrogen evolution in the presence of methanol over Fe(2.5%)-CeO_2 RM under visible light.

Under visible light, the electrons promoted in the CB are able to reduce protons generating hydrogen since the E_{CB} value (-0.75 V vs NHE at pH=7) is more negative than the H^+/H_2 reduction potential (-0.413 V vs NHE at pH=7 [85, 86]) whereas, being the E_{VB} value (+2.04 V vs NHE at pH=7) less positive than the $^{\bullet}OH/H_2O$ pair (+2.31 V vs NHE at pH=7 [87]), the positive holes in the VB cannot

generate hydroxyls from water. On the other hand, the positive holes are able to oxidize methanol and its oxidation products since the E_{VB} value of the photocatalyst is deeper than the redox potentials of HCHO/CH_3OH (-0.213 V vs NHE at pH=7 [85]), HCOOH/HCHO (-0.363 V vs. NHE at pH=7 [85]) and CO_2/HCOOH (-0.613 V vs. NHE at pH=7 [86]).

Based on the results reported in Fig. 14 and considering the scheme of band alignment and redox potentials of the involved chemical species presented in Fig. 15, a possible reaction pathway has been proposed.

$$Fe(2.5\%) - CeO_2\ RM \xrightarrow{h\nu} e^- + h^+ \quad \text{R1}$$

$$CH_3OH + h^+ \rightarrow \ oxidation\ products\ (HCOH, HCOOH,\ CO_2) + H^+ \quad \text{R2}$$

$$2H_2O + 4h^+ \rightarrow\ 4H^+ +\ O_2 \quad \text{R3}$$

$$2H^+ +\ 2e^- \rightarrow H_2 \quad \text{R4}$$

When the Fe(2.5%)-CeO_2 RM is irradiated by visible light, electrons are promoted from the VB to CB, generating positive holes in the VB (R1). Thereafter, the positive holes preferentially oxidize methanol (R2) to form HCOH, which is further oxidized to HCOOH [88, 89]. Subsequently, HCOOH is decarboxylated via the photo-Kolbe reaction to produce CO_2 [90]. Simultaneously, the electrons in the CB can produce H_2 from H^+ (R4) coming the water oxidation (R3) and, to a certain extent, also from the methanol oxidation pathway (R2).

3.5 Comparison with the available literature

Table 4 shows a comparison between the results obtained in the present work in terms of H_2 production and the literature data on the photocatalytic hydrogen production obtained from CeO_2-based catalysts active under visible light. It should be specified that, since the data reported in the literature refers to light sources characterized by different electric power (W), in order to make a

homogeneous comparison, the data in terms of hydrogen evolution rate (μmol h^{-1}) were normalized to the electric power of the light source used in the photocatalytic experiments.

Photocatalyst	**Visible light source**	**Sacrificial agent**	**Normalized H_2 evolution rate (μmol h^{-1} W^{-1})**	**Reference**
CeO_2/MoS_2	150 W Xenon arc lamp (>400 nm)	Na_2SO_3/Na_2S	1.6	[91]
Fe-doped CeO_2	125 W medium pressure Hg lamp (λ ≥ 400 nm)	Methanol	5.1	[31]
$CeO_2/ZnIn_2S_4$	300 W Xe lamp (λ > 420 nm)	Methanol	0.11	[92]
$SnIn_4S_8/CeO_2$	300 W Xenon lamp with a UV cut-off filter (λ > 420 nm)	Triethanolamine	0.103	[93]
CdS-Pt@CeO_2	300W Xe lamp (λ > 420 nm)	Lactic acid	5.3	[94]
Pt/CeO_2/g-C_3N_4	300 W Xe lamp with 420 nm cut-off filter	Triethanolamine	0.16	[95]
CeO_2/Ultrathin MXene	300 W Xe lamp with 400 nm cut-off filter	Triethanolamine	0.045	[96]
CeO_2/CdSe-Diethylenetriamine	300 W Xe lamp with 420 nm cut-off filter	Na_2SO_3/Na_2S	0.62	[97]

Fe(2.5%)-CeO_2 RM	Four 8 W visible lamps (emission: 400-700 nm)	Methanol	4.9	Present work

Table 4. Comparison with the literature dealing with CeO_2-based photocatalysts for hydrogen evolution under visible light

The results show that the normalized photocatalytic hydrogen evolution rate obtained with Fe(2.5%)-CeO_2 RM (4.9 μmol h^{-1} W^{-1}) is much higher than the literature data, except in the case reported by You et al. (5.3 μmol h^{-1} W^{-1}) [94] and Mansingh et al. (5.1 μmol h^{-1} W^{-1}) [31], which showed similar results to that obtained with Fe(2.5%)-CeO_2 RM. However, it should be specified that in the case of the work by You et al., the use of a catalyst containing Pt is foreseen [94]. Furthermore, in the case of the paper by Mansingh et al., a calcination step (treatment at high temperatures) is necessary to prepare the Fe-doped CeO_2 photocatalyst [31]. Noticeably, it seems that, from the chemical-physical characterization data reported by the same authors (in particular the UV-Vis absorbance data), the sample at the optimal iron amount (3 wt%) also contains a fraction of iron oxides on the photocatalyst surface, indicating that the adopted method is not able to effectively dope the CeO_2 lattice with iron.

4 Conclusions

In this work, Fe-doped CeO_2 photocatalysts at different iron content were prepared via the reverse micelle (RM) preparation route and tested, for the first time, in the visible-light-driven hydrogen production from methanol aqueous solutions. The effectiveness of the preparation method in improving structural, optical, and textural properties was highlighted by comparison with Fe-CeO_2 systems prepared by conventional precipitation. The aforementioned comparison was conducted with the benefit of in-depth characterization through complementary techniques. XRD and TEM results proved that precipitation in the confined space generated by the reverse micelles effectively generated ultra-small (around 4 nm) photocatalyst nanocrystals. Remarkable is the improvement in optical properties obtained exclusively with the RM system, which favors the effective inclusion of

heteroatoms in large quantities with the possibility of altering the band gap with iron content, increasing the average lifetime of excitons, and tuning the concentration of Ce^{3+} and Vo defects, as evidenced by Raman, UV-Vis, and photoluminescence spectroscopies. Outstanding values of surface area were achieved by RM compared to conventional methods.

Photocatalytic activity data of RM samples revealed that the highest hydrogen production (7566 μmol L^{-1}) was obtained when the iron content in the CeO_2 lattice was increased from 1 up to 2.5 mol%, which is hence to be considered the optimal value for the CeO_2 doping by reverse micelle route. Fe(2.5%)-CeO_2 RM is the best trade-off between the extent of substitutional doping and the generation of defects consisting of oxygen vacancies. The latter, in turn, results in a suitable band gap value and a delay in charge carrier recombination. In addition, a larger pore volume of the photocatalyst favors the diffusion phenomena of the reagents toward the active sites

Photocatalytic test results were critically discussed in correlation with the physicochemical properties of the prepared materials, evidencing that the hydrogen evolution rate under visible light is mainly linked to the ability of Fe-doped CeO_2 to reduce the recombination rate of electron-hole pairs and to the photocatalysts total pore volume. The stability of the optimally doped photocatalyst was investigated, showing no significant change in the photocatalytic hydrogen production after six reuse cycles. Moreover, the possible visible-light-driven photocatalytic mechanism related to the hydrogen evolution from methanol aqueous solution was established based on the photocatalytic results obtained using D_2O and considering the band alignment scheme together with the redox potentials of the involved chemical species. In detail, it was evidenced that hydrogen was produced from the reduction of H^+ by the electrons promoted in the conduction band while methanol was preferentially oxidized by the photogenerated positive holes. The impact of the preparation route for Fe-doped CeO_2 doped with the optimal iron content (2.5 mol%) was finally investigated. The Fe-doped CeO_2 photocatalyst prepared by the reverse micelle route showed a photocatalytic hydrogen production better than the doped sample prepared by the conventional precipitation method. The enhanced photocatalytic performance for the photocatalyst prepared by the reverse micelle method was mainly

ascribed to the extended stability of photogenerated electron-hole pairs (i.e. the decrease in the recombination rate), assuring a longer lifetime of electrons promoted in the conduction band and hence an improvement of photocatalytic hydrogen production.

Acknowledgments

"B.M. is indebted to Prof. JM Bluet for his help during the Raman spectrometry measurements". Transmission Electron Microscope (TEM) was purchased with funding from the "Ministero dell'Università e della Ricerca (MUR)" (Italy) under the "Dipartimento di Eccellenza 2018–2022" program.

References

[1] T. Hisatomi, J. Kubota, K. Domen, Chem. Soc. Rev. 43 (2014) 7520-7535.
[2] G. Vitiello, L. Clarizia, W. Abdelraheem, S. Esposito, B. Bonelli, N. Ditaranto, A. Vergara, M. Nadagouda, D.D. Dionysiou, R. Andreozzi, ChemCatChem 11 (2019) 4314-4326.
[3] O. Vozniuk, N. Tanchoux, J.-M. Millet, S. Albonetti, F. Di Renzo, F. Cavani, Stud. Surf. Sci. Catal., Elsevier, 2019, pp. 281-302.
[4] M. Wang, S. Shen, L. Li, Z. Tang, J. Yang, J. Mater. Sci. 52 (2017) 5155-5164.
[5] K. Maeda, J. Photochem. Photobiol., C 12 (2011) 237-268.
[6] X. Wang, W.-c. Peng, X.-y. Li, Int. J. Hydrogen Energy 39 (2014) 13454-13461.
[7] C.R. López, E.P. Melián, J.O. Méndez, D.E. Santiago, J.D. Rodríguez, O.G. Díaz, J. Photochem. Photobiol., A 312 (2015) 45-54.
[8] K.C. Christoforidis, P. Fornasiero, ChemCatChem 9 (2017) 1523-1544.
[9] X. Chen, S. Shen, L. Guo, S.S. Mao, Chem. Rev. 110 (2010) 6503-6570.
[10] X. Wang, K. Maeda, A. Thomas, K. Takanabe, G. Xin, J.M. Carlsson, K. Domen, M. Antonietti, Nat. Mater. 8 (2009) 76-80.
[11] G. Iervolino, V. Vaiano, D. Sannino, L. Rizzo, V. Palma, Appl. Catal., B 207 (2017) 182-194.
[12] G. Iervolino, V. Vaiano, J. Murcia, L. Rizzo, G. Ventre, G. Pepe, P. Campiglia, M. Hidalgo, J.A. Navío, D. Sannino, J. Catal. 339 (2016) 47-56.
[13] G. Iervolino, V. Vaiano, J. Murcia, A. Lara, J. Hernández, H. Rojas, J. Navío, M. Hidalgo, Int. J. Hydrogen Energy 46 (2021) 38678-38691.
[14] A. Kudo, Y. Miseki, Chem. Soc. Rev. 38 (2009) 253-278.
[15] F.E. Osterloh, Chem. Mater. 20 (2008) 35-54.
[16] A. Mancuso, N. Morante, M. De Carluccio, O. Sacco, L. Rizzo, M. Fontana, S. Esposito, V. Vaiano, D. Sannino, Chem. Eng. J. 450 (2022) 138107.
[17] A. Mancuso, N. Blangetti, O. Sacco, F.S. Freyria, B. Bonelli, S. Esposito, D. Sannino, V. Vaiano, Nanomaterials 13 (2023) 270.
[18] O. Sacco, J. Murcia, A. Lara, M. Hernández-Laverde, H. Rojas, J. Navío, M. Hidalgo, V. Vaiano, Mater. Sci. Semicond. Process. 107 (2020) 104839.

[19] A. Mancuso, O. Sacco, D. Sannino, S. Pragliola, V. Vaiano, Arabian J. Chem. 13 (2020) 8347-8360.
[20] J. Low, J. Ma, J. Wan, W. Jiang, Y. Xiong, Acc. Mater. Res. 3 (2021) 331-342.
[21] K. Chen, F. Qu, Y. Huang, J. Cai, F. Wu, W. Li, Advanced Nanocomposites (2024).
[22] A. Mancuso, G. Iervolino, Catalysts 12 (2022) 1074.
[23] C. Sun, H. Li, L. Chen, Energy Environ. Sci. 5 (2012) 8475-8505.
[24] O. Tammaro, R. Paparo, M. Chianese, I. Ritacco, L. Caporaso, M.F. Camellone, B. Masenelli, A.D. Lamirand, J.-M. Bluet, M. Fontana, G. Pinto, A. Illiano, A. Amoresano, M. Di Serio, V. Russo, S. Esposito, Chem. Eng. J. 479 (2024) 147909.
[25] M.K. Chinnu, P. Anandan, M. Arivanandhan, A. Venkatesan, R.M. Kumar, R. Jayavel, J. Mater. Sci.: Mater. Electron. 29 (2018) 9564-9572.
[26] A. Fauzi, A. Jalil, N. Hassan, F. Aziz, M. Azami, I. Hussain, R. Saravanan, D.-V. Vo, Chemosphere 286 (2022) 131651.
[27] Z. Shen, Y. Zhou, Y. Guo, J. Zhao, J. Song, Y. Xie, Y. Ling, W. Zhang, Chin. Chem. Lett. 32 (2021) 2524-2528.
[28] M. Wang, M. Shen, X. Jin, J. Tian, Y. Shao, L. Zhang, Y. Li, J. Shi, Chem. Eng. J. 427 (2022) 130987.
[29] K. Yang, D.-F. Li, W.-Q. Huang, L. Xu, G.-F. Huang, S. Wen, Appl. Phys. A 123 (2017) 1-11.
[30] H. Yang, L. Jia, Z. Zhang, B. Xu, Q. Zhang, S. Yuan, Y. Xiao, Z. Nan, M. Zhang, Y. Zhang, Appl. Mater. Today 29 (2022) 101651.
[31] S. Mansingh, D. Padhi, K. Parida, Int. J. Hydrogen Energy 41 (2016) 14133-14146.
[32] F. Heidari, A. Irankhah, Ceram. Int. 40 (2014) 12655-12660.
[33] S. Esposito, in: S. Esposito (Ed.), Sol-Gel Synthesis Strategies for Tailored Catalytic Materials, Springer International Publishing, Cham, 2023, pp. 43-51.
[34] M. Pileni, J. Phys. Chem. 97 (1993) 6961-6973.
[35] B. Bonelli, O. Tammaro, F. Martinovic, R. Nasi, G. Dell'Agli, P. Rivolo, F. Giorgis, N. Ditaranto, F.A. Deorsola, S. Esposito, ACS Omega 6 (2021) 24562-24574.
[36] R. Nasi, S. Esposito, F.S. Freyria, M. Armandi, T.A. Gadhi, S. Hernandez, P. Rivolo, N. Ditaranto, B. Bonelli, Materials 12 (2019) 937.
[37] J. Han, J. Meeprasert, P. Maitarad, S. Nammuangruk, L. Shi, D. Zhang, J. Phys. Chem. C 120 (2016) 1523-1533.
[38] S. Ghosh, J. Colloid Interface Sci. 360 (2011) 672-680.
[39] V. Vaiano, M. Matarangolo, O. Sacco, D. Sannino, Appl. Catal., B 209 (2017) 621-630.
[40] K. Kočí, M. Reli, M. Edelmannová, I. Troppová, H. Drobná, A. Rokicińska, P. Kuśtrowski, D. Dvoranová, L. Čapek, J. Photochem. Photobiol., A 366 (2018) 55-64.
[41] P. Udani, M. Rønning, Oil Gas Sci. Technol. 70 (2015) 831-839.
[42] S. Esposito, Sol-Gel Synthesis Strategies for Tailored Catalytic Materials, Springer, 2023, pp. 53-71.
[43] A.K. Lucid, P.R. Keating, J.P. Allen, G.W. Watson, J. Phys. Chem. C 120 (2016) 23430-23440.
[44] D.E. Vanpoucke, P. Bultinck, S. Cottenier, V. Van Speybroeck, I. Van Driessche, J. Mater. Chem. A 2 (2014) 13723-13737.
[45] N.S. Arul, D. Mangalaraj, P.C. Chen, N. Ponpandian, C. Viswanathan, Mater. Lett. 65 (2011) 2635-2638.
[46] H. Liu, Y. Wu, L. Liu, B. Chu, Z. Qin, G. Jin, Z. Tong, L. Dong, B. Li, Appl. Surf. Sci. 498 (2019) 143780.
[47] M. Balestrieri, S. Colis, M. Gallart, G. Schmerber, M. Ziegler, P. Gilliot, A. Dinia, J. Mater. Chem. C 3 (2015) 7014-7021.
[48] J. Calvache-Muñoz, F.A. Prado, L. Tirado, L.C. Daza-Gomez, G. Cuervo-Ochoa, H.L. Calambas, J.E. Rodríguez-Páez, J. Inorg. Organomet. Polym. Mater. 29 (2019) 813-826.

[49] A. Nikolic, M. Boskovic, M. Fabian, D. Bozanic, M. Vucinic-Vasic, A. Kremenovic, B. Antic, J. Nanosci. Nanotechnol. 13 (2013) 6787-6792.
[50] A. Mancuso, O. Sacco, V. Vaiano, B. Bonelli, S. Esposito, F.S. Freyria, N. Blangetti, D. Sannino, Materials 14 (2021) 3105.
[51] P. Webb, C. Orr, R. Camp, J. Oliver, Y. Yunes, Norcross: Micromeritics Instrument Corporation.
[52] Z. Popović, Z. Dohčević-Mitrović, N. Paunović, M. Radović, Phys. Rev. B: Condens. Matter 85 (2012) 014302.
[53] S.N. Matussin, F. Khan, M.H. Harunsani, Y.-M. Kim, M.M. Khan, ACS Omega 8 (2023) 11868-11879.
[54] B. Xu, H. Yang, Q. Zhang, S. Yuan, A. Xie, M. Zhang, T. Ohno, ChemCatChem 12 (2020) 2638-2646.
[55] H. Bao, K. Qian, J. Fang, W. Huang, Appl. Surf. Sci. 414 (2017) 131-139.
[56] V. Paidi, N. Ferreira, D. Goltz, J. Van Lierop, J. Phys.: Condens. Matter 27 (2015) 336001.
[57] F. Zhang, P. Wang, J. Koberstein, S. Khalid, S.-W. Chan, Surf. Sci. 563 (2004) 74-82.
[58] H. Idriss, Surf. Sci. 712 (2021) 121894.
[59] Y. Huang, Y. Yu, Y. Yu, B. Zhang, Sol. RRL 4 (2020) 2000037.
[60] A. Corma, P. Atienzar, H. García, J.-Y. Chane-Ching, Nat. Mater. 3 (2004) 394-397.
[61] Y.S. Chaudhary, S. Panigrahi, S. Nayak, B. Satpati, S. Bhattacharjee, N. Kulkarni, J. Mater. Chem. 20 (2010) 2381-2385.
[62] L. Nadjia, E. Abdelkader, B. Naceur, B. Ahmed, J. Rare Earths 36 (2018) 575-587.
[63] A. Kadam, T.G. Kim, D.S. Shin, K. Garadkar, J. Park, J. Alloys Compd. 710 (2017) 102-113.
[64] D. Channei, B. Inceesungvorn, N. Wetchakun, S. Ukritnukun, A. Nattestad, J. Chen, S. Phanichphant, Sci. Rep. 4 (2014) 5757.
[65] A.K. Sahu, X.S. Zhao, S. Upadhyayula, Catal. Rev. (2023) 1-78.
[66] J.-w. Shi, X. Yan, H.-J. Cui, X. Zong, M.-L. Fu, S. Chen, L. Wang, J. Mol. Catal. A: Chem. 356 (2012) 53-60.
[67] L. Zhang, Y. Zhu, Y. He, W. Li, H. Sun, Appl. Catal., B 40 (2003) 287-292.
[68] S.-C. Jung, S.-J. Kim, N. Imaishi, Y.-I. Cho, Appl. Catal., B 55 (2005) 253-257.
[69] X. You, F. Chen, J. Zhang, J. Sol-Gel Sci. Technol. 34 (2005) 181-187.
[70] J.-w. Shi, J.-t. Zheng, P. Wu, J. Hazard. Mater. 161 (2009) 416-422.
[71] E. Gaggero, P. Calza, E. Cerrato, M.C. Paganini, Catalysts 11 (2021) 1520.
[72] O. Sacco, P. Franco, I. De Marco, V. Vaiano, E. Callone, R. Ceccato, F. Parrino, J. Mater. Sci. Technol. 112 (2022) 49-58.
[73] S. Esposito, Sol-Gel Synthesis Strategies for Tailored Catalytic Materials, Springer, 2023.
[74] L. Katta, G. Thrimurthulu, B.M. Reddy, M. Muhler, W. Grünert, Catal. Sci. Technol. 1 (2011) 1645-1652.
[75] A. Ramírez, L. Sierra, M. Mesa, J. Restrepo, Chem. Eng. Sci. 60 (2005) 4702-4708.
[76] R.R. Guimaraes, A.L. Parussulo, K. Araki, Electrochim. Acta 222 (2016) 1378-1386.
[77] J. Pan, S. Wang, A. Chen, Y. Chen, M. Wang, Y. Chen, J. Alloys Compd. 898 (2022) 162895.
[78] M. Shaban, A.M. Ahmed, N. Shehata, M.A. Betiha, A.M. Rabie, J. Colloid Interface Sci. 555 (2019) 31-41.
[79] H. Belhadj, S. Hamid, P.K. Robertson, D.W. Bahnemann, ACS Catal. 7 (2017) 4753-4758.
[80] S.-i. Fujita, H. Kawamori, D. Honda, H. Yoshida, M. Arai, Appl. Catal., B 181 (2016) 818-824.
[81] T. Chen, Z. Feng, G. Wu, J. Shi, G. Ma, P. Ying, C. Li, J. Phys. Chem. C 111 (2007) 8005-8014.
[82] B.P. Nenavathu, S. Kandula, S. Verma, RSC Adv. 8 (2018) 19659-19667.
[83] D. Channei, K. Chansaenpak, S. Phanichphant, P. Jannoey, W. Khanitchaidecha, A. Nakaruk, ACS Omega 6 (2021) 19771-19777.
[84] E.A. Abdullah, Eur. J. Chem. 10 (2019) 82-94.

[85] P. Gomathisankar, K. Hachisuka, H. Katsumata, T. Suzuki, K. Funasaka, S. Kaneco, Int. J. Hydrogen Energy 38 (2013) 11840-11846.
[86] C.Y. Toe, C. Tsounis, J. Zhang, H. Masood, D. Gunawan, J. Scott, R. Amal, Energy Environ. Sci. 14 (2021) 1140-1175.
[87] L. Wang, Q. Zhang, B. Chen, Y. Bu, Y. Chen, J. Ma, F.L. Rosario-Ortiz, R. Zhu, Water Res. 174 (2020) 115605.
[88] G. BAMWENDA, A.M. MIKA, T.Z. WINNICKI, Environ. Prot. Eng. 16 (1990).
[89] Q. Shi, X. Wei, A. Raza, G. Li, ChemCatChem 13 (2021) 3381-3395.
[90] C. Tao, W. Guopeng, F. Zhaochi, H. Gengshen, S. Weiguang, Y. Pinliang, L. Can, Chin. J. Catal. 29 (2008) 105-107.
[91] A.A. Yadav, Y.M. Hunge, S.-W. Kang, Catalysts 12 (2022) 1185.
[92] R. Jiang, L. Mao, Y. Zhao, J. Zhang, E.B. Chubenko, V. Bondarenko, Y. Sui, X. Gu, X. Cai, Sci. China Mater. 66 (2023) 139-149.
[93] C.-H. Shen, Y. Chen, X.-J. Xu, X.-Y. Li, X.-J. Wen, Z.-T. Liu, R. Xing, H. Guo, Z.-H. Fei, J. Hazard. Mater. 416 (2021) 126217.
[94] D. You, B. Pan, Y. He, X. Wang, W. Su, Res. Chem. Intermed. 43 (2017) 5103-5112.
[95] W. Zou, Y. Shao, Y. Pu, Y. Luo, J. Sun, K. Ma, C. Tang, F. Gao, L. Dong, Appl. Catal., B 218 (2017) 51-59.
[96] H. Zhu, X. Fu, Z. Zhou, ACS Omega 7 (2022) 21684-21693.
[97] Z. Li, D. Jin, Z. Wang, Int. J. Hydrogen Energy 46 (2021) 6358-6368.

Graphical Abstract

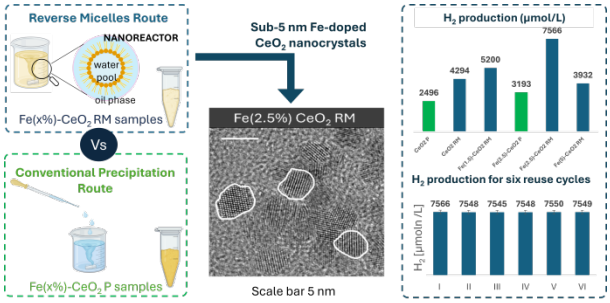

The reverse micelles route allows for obtaining sub-5 nm Fe-doped CeO_2 catalysts for hydrogen photoproduction under visible light with high stability and remarkable photoactivity compared to the conventional precipitation method.